TECHNOLOGY FOR SUSTAINED SUPERSONIC COMBUSTION

Task Order 0006: Scramjet Research with Flight-Like Inflow Conditions

John Boles and Ryan Milligan

Taitech, Inc.

JANUARY 2013
Final Report

STINFO COPY

AIR FORCE RESEARCH LABORATORY
AEROSPACE SYSTEMS DIRECTORATE
WRIGHT-PATTERSON AIR FORCE BASE, OH 45433-7542
AIR FORCE MATERIEL COMMAND
UNITED STATES AIR FORCE

NOTICE AND SIGNATURE PAGE

*//Signature//
STEPHEN K. SMITH
Hypersonic Sciences Branch
High Speed Systems Division
Aerospace Systems Directorate

//Signature//
MARK A. AMENDT, Maj, USAF
Chief, Hypersonic Sciences Branch
High Speed Systems Division
Aerospace Systems Directorate

//Signature//
ROBERT A. MERCIER
Deputy for Technology
High Speed Systems Division
Aerospace Systems Directorate

REPORT DOCUMENTATION PAGE

The public reporting burden for this collection of information is estimated to average 1 hour per response, including the time for reviewing instructions, searching existing data sources, gathering and maintaining the data needed, and completing and reviewing the collection of information. Send comments regarding this burden estimate or any other aspect of this collection of information, including suggestions for reducing this burden, to Department of Defense, Washington Headquarters Services, Directorate for Information Operations and Reports (0704-0188), 1215 Jefferson Davis Highway, Suite 1204, Arlington, VA 22202-4302. Respondents should be aware that notwithstanding any other provision of law, no person shall be subject to any penalty for failing to comply with a collection of information if it does not display a currently valid OMB control number. **PLEASE DO NOT RETURN YOUR FORM TO THE ABOVE ADDRESS**.

1. REPORT DATE *(DD-MM-YY)*	2. REPORT TYPE	3. DATES COVERED *(From - To)*
January 2013	Final	13 July 2011 – 13 January 2013

4. TITLE AND SUBTITLE

TECHNOLOGY FOR SUSTAINED SUPERSONIC COMBUSTION
Task Order 0006: Scramjet Research with Flight-Like Inflow Conditions

5a. CONTRACT NUMBER
FA8650-08-D-2844-0006

5b. GRANT NUMBER

5c. PROGRAM ELEMENT NUMBER
62203F

6. AUTHOR(S)

John Boles and Ryan Milligan

5d. PROJECT NUMBER
3012

5e. TASK NUMBER
N/A

5f. WORK UNIT NUMBER
Q09D

7. PERFORMING ORGANIZATION NAME(S) AND ADDRESS(ES)

Taitech, Inc.
1430 Oak Court, Suite 301
Beavercreek, OH 45430-1065

8. PERFORMING ORGANIZATION REPORT NUMBER

9. SPONSORING/MONITORING AGENCY NAME(S) AND ADDRESS(ES)

Air Force Research Laboratory
Aerospace Systems Directorate
Wright-Patterson Air Force Base, OH 45433-7542
Air Force Materiel Command
United States Air Force

10. SPONSORING/MONITORING AGENCY ACRONYM(S)
AFRL/RQHF

11. SPONSORING/MONITORING AGENCY REPORT NUMBER(S)
AFRL-RQ-WP-TR-2013-0029

12. DISTRIBUTION/AVAILABILITY STATEMENT

Approved for public release; distribution unlimited.

13. SUPPLEMENTARY NOTES

PA Case Number: 88ABW-2013-2922; Clearance Date: 18 Jun 2013. This report contains color.

14. ABSTRACT

This report focuses on the impact of shock distortion on various high-speed flows for scramjet applications. Simulations consist of shocked sonic injection into a supersonic crossflow, shock distorted cavity-assisted fuel mixing and combustion, and novel experimental designs. Hybrid large eddy simulation/Reynolds-averaged Navier-Stokes (LES/RANS) turbulence modeling techniques are highlighted and their ability to capture the unsteady nature of high-speed turbulent flows is investigated. This task provided extended experience and knowledge of using hybrid LES/RANS techniques for internal high-speed flows. These results also will provide valuable information for better understanding the complicated physics of shock boundary layer interactions and mixing in high-speed flows in detail that experiments cannot easily provide.

15. SUBJECT TERMS

scramjet, fuel injection, mixing, turbulence modeling, hybrid LES/RANS, unsteady, shock distortion, combustion modeling

16. SECURITY CLASSIFICATION OF:			17. LIMITATION OF ABSTRACT:	18. NUMBER OF PAGES	19a. NAME OF RESPONSIBLE PERSON (Monitor)
a. REPORT	**b. ABSTRACT**	**c. THIS PAGE**	SAR	80	Stephen K. Smith
Unclassified	Unclassified	Unclassified			**19b. TELEPHONE NUMBER** *(Include Area Code)* N/A

Table of Contents

List of Figures

List of Tables

1 Summary

This report covers work done under Task Order 0006 of Contract FA8650-08-D-2844, with a focus on computational fluid dynamics (CFD) simulations to improve the understanding of high-speed internal flows for scramjet applications. A large focus of this effort is on the effect of shock distortion on fundamental scramjet flows. This work also focuses on broadening the applicability of the higher-fidelity hybrid Large Eddy Simulation/Reynolds-Averaged Navier-Stokes (LES/RANS) methodology to larger and more complex problems.

The first major topic covered in this report is that of shock-distorted injection. This work simulates the experiments at the Air Force Research Laboratory (AFRL) where an oblique shock impinged upon a simple flush wall injector and involved only cold mixing flow without combustion. The purpose of this experiment was to understand the effects of shock waves formed by the inlet of a scramjet in the context of a direct connect wind tunnel. RANS and hybrid LES/RANS simulations of these experiments showed the capability of those methodologies to simulate the impact of this shockwave-boundary layer interaction (SBLI) on mixing flows.

The shock distortion concept was extended to a more complex flow of cavity mixing and then cavity combustion. Again in coordination with an experimental effort at AFRL, RANS and LES/RANS simulations were performed to simulate these experimental efforts as well as to assist in the design of the experiment.

Two smaller studies were also performed. The first is analysis of a conceptual nearly-round isolator which could provide flow similar to a fully-round isolator but with two flat edges to better accomodate optical diagnostics. A simple mixing flow in this conceptual flowpath is compared to round and rectangular flowpaths. This concept shows promise to provide simpler diagnostic access for round flowpaths.

The second smaller study is analysis of a shock distortion generator for a round cross-section. The report details multiple design iterations with descriptions of the reasons for design changes. A set of design criteria is presented and each design is judged based on these performance criteria.

2 Introduction

In the continuing effort to better understand hypersonic flow phenomena, mixing characteristics of various fuels and fueling strategies are a critical part. Knowledge of the mixing characteristics is obtained from experimental and computational approaches. The present work focuses on the computational approach, but includes interaction with the experimental efforts in the Air Force Research Laboratory wind tunnels.

An aspect of scramjet physics that needs further investigation is the role of flow distortion caused by oblique shock from the cowl in real scramjet flows (such as that in Figure 1). In typical direct connect wind tunnel facilities, the flow is nearly uniform coming out of the facility nozzle – completely missing the impact of this cowl shock. Studies have shown [1,2] that these shocks have significant impact on mixing and plume structures.

Reynolds-Averaged Navier Stokes (RANS) simulations have proved to be adequate for predicting penetration heights, but have not typically been as successful at predicting lateral spreading, vortical structures within plumes, or mixing within the core of injectant plumes [4–6]. Large Eddy Simulation (LES) and Direct Numerical Simulation (DNS) methods have shown success in predicting many turbulent flows, but are very expensive computationally for wall-bounded high Reynolds number flows, as the turbulent scales that need to be resolved by the grid become very small. Hybrid methods [7–9] have been developed to use LES for the majority of the flowfield and use RANS near solid surfaces, where the turbulent length scales are small. Both RANS and hybrid LES/RANS approaches are applied in the current studies, and these methods are described more fully in Section 3.

Section 4.1 describes the investigations of an oblique shock wave impacting on jet injection into a supersonic crossflow. Injection normal to the wall is a common approach to obtain good fuel penetration, and the penetration characteristics with uniform inflows have been well characterized [10,11]. The present computational studies were carried out with a complimentary experimental study with the AFOSR efforts of Cam Carter to assess the impact of shocks on the fuel penetration and mixing.

Section 4.2 documents computational studies of cavity flameholders in the presence of distorted inflows. Cavities are often used to stabilize supersonic combustion by inducing separation within [12,13]. Steady-state numerical investigations of cavity flameholders have been performed regularly in the past using steady-state methods [14,15] but only in recent years have computational resources allowed for the simulation of these flows with unsteady LES and LES/RANS methods. In addition, the impact of flow distortion caused by oblique shocks from the cowl in scramjet flowpaths is of interest. Section 4.2 discusses the impact of an oblique shock impinging in the region of a cavity flameholder. For mixing flows, computational studies were performed with both RANS and hybrid LES/RANS, while only RANS was used for combusting flows.

Section 4.3 compares mixing characteristics for sonic injection into a supersonic crossflow, for rectangular, round, and nearly-round cross-sections. Both rectangular and round cross-sections are of technical interest, but optical access for round cross-sections is limited due to the complexity of round windows that can distort optical
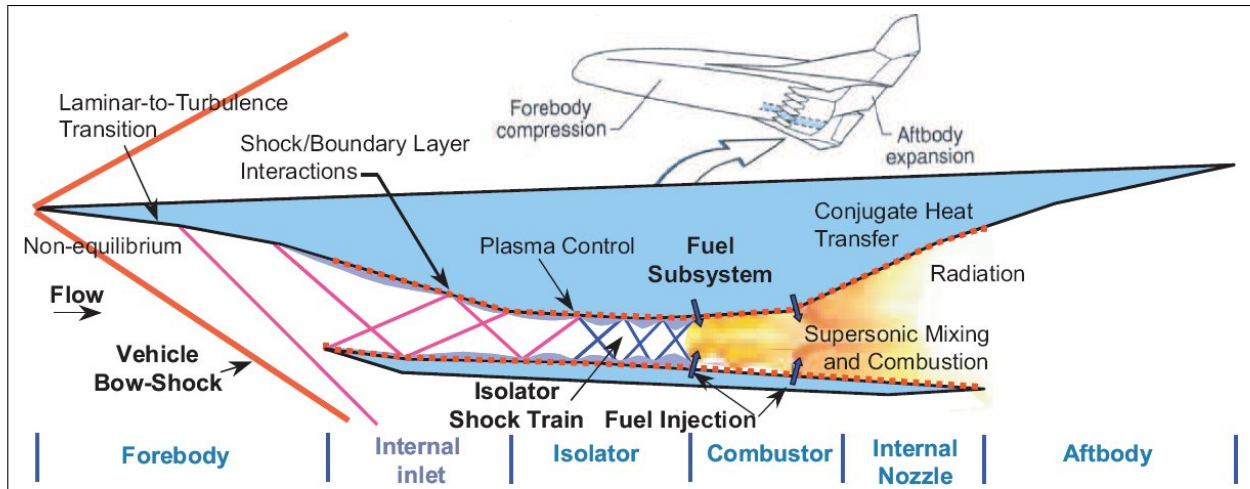
Figure 1: Idealized Scramjet Flowpath Diagram

(Image from NASA [3])

measurements. Hence, a nearly round-cross-section, which was derived by removing an arc of the full round cross-section, was studied to see how this geometric compromise would affect the mixing characteristics.

Section 4.4 presents analysis of distortion generation for round cross-sections. The purpose is to mimic the distortion that would propagate into an isolator from an inlet of a flight vehicle. Prior research on distortion for round cross-sections has focused on air injection, but this leads to an undesireable thermal distortion created by the injected air. The work described here focuses on intrusive devices that do not create the thermal distortion.

3 Methods, Assumptions, and Procedures

3.1 REACT-MB for Hybrid LES/RANS and RANS Simulations

A hybrid LES/RANS method was developed at North Carolina State University's Aerospace Engineering CFD Lab [16] for use with their REACT-MB flow solver in hypersonic flow applications. It uses RANS as a near-wall method that smoothly transitions to LES in the boundary layer where the logarithmic layer deviates from the wake law in a time-averaged sense. This method has been successful in predicting Mach 2 crossflow cases with air, helium and ethylene injection [5].

The REACT-MB hybrid LES/RANS formulation was used for some of the simulations shown in this work. The hybrid method [17] combines a Menter BSL RANS model near the wall with a Smagorinsky subgrid model away from the wall. The transition from LES to RANS is accomplished by a blending function based on the ratio of the closest wall distance to a modeled form of the Taylor microscale. An unsteady inflow condition was provided using a recycling and rescaling routine which is detailed in earlier work [17]. RANS simulations with REACT-MB utilized the Menter BSL model for the turbulent fluxes. Inviscid fluxes are discretized using Edwards' Low-Diffusion Flux-Splitting Scheme (LDFSS) [18] and viscous and diffusive fluxes used second-order central differences. The Piecewise Parabolic Method (PPM) of Colella and Woodward [19] was used to extend LDFSS to higher order accuracy.

3.2 CFD++ for RANS Simulations

RANS simulations were performed using the CFD++ code, a general-purpose CFD tool developed by Metacomp Technologies [20]. CFD++ uses a finite-volume numerical framework, with multi-dimensional Total Variation Diminishing (TVD) schemes and Riemann solvers for accurate representation of supersonic flows. Several types of Riemann solver are available; the Harten-Lax-van Leer-Contact (HLLC) Riemann solver with minmod flux limiting was used in the simulations described here. Multi-grid acceleration is available to provide a fast and accurate solution methodology for both steady and unsteady flows. A variety of one-, two-, and three-equation turbulence models are available for RANS calculations, along with large eddy simulation (LES) and hybrid RANS/LES options. In all the cases presented here, turbulence was modeled using the two-equation cubic $k - \epsilon$ model. This model has non-linear terms that account for normal-stress anisotropy, swirl, and streamline-curvature effects. At solid surfaces, an advanced two-layer wall function with equilibrium and nonequilibrium blending was employed to reduce grid requirements. The code supports both structured (quadrilateral and hexahedral) and unstructured (triangle, prism, and tetrahedral) grids. A Message Passing Interface (MPI) is used to take advantage of modern parallel-processing computers.

4 Results and Discussion

The four studies addressed in this effort are described individually in the sections below. The first subsection describes LES/RANS analysis of the effects of shocks on injection into a supersonic crossflow. The second focuses on LES/RANS analysis of shock effects on non-reacting flows over cavity flameholders, and on RANS analysis of reacting flows over cavity flameholders. The third subsection focuses on jet injection into supersonic flows in nearly-round cross-sections, while the fourth describes development of techniques to create flight-like flow distortion in a direct-connect environment.

4.1 Shocked Injection

An aspect of scramjet physics that needs further investigation is the role of flow distortion caused by oblique shock from the cowl in real scramjet flows (such as that in Figure 1). In typical direct connect wind tunnel facilities, the flow is nearly uniform coming out of the facility nozzle – completely missing the impact of this cowl shock. Studies have shown [1, 2] that these shocks have significant impact on mixing and plume structures. This section discusses the experimental study of an oblique shock impinging downstream of a normal injector, followed by a description of the hybrid LES/RANS simulations and comparison to the experimental observations.

An experimental investigation of the impact of oblique shock waves on normal jet injection of air has been conducted to complement the computational studies being performed. The tunnel conditions and jet conditions mimic those used in prior studies [10, 11] of normal jet injection. A single circular jet with a jet diameter (D) of $3/16$ inch was located in the bottom wall of the tunnel, approximately 5.9 inch from the end of the Mach 2 facility nozzle of Research Cell 19 at the Air Force Research Laboratory [21]. On the upper wall, a beveled plate was mounted, which could be translated axially. The leading bevel turned the flow by either 5 or 7 degrees, before turning back parallel to the lower wall. The shock generator thickness was $3/8$ inch. During calibration runs, a shadowgraph system was used to verify the position of the shock relative to the injector.

Following the calibration runs the shadowgraph system was replaced by an nitrous oxide planar laser-induced fluorescence (NO-PLIF) system. NO-PLIF images were obtained on spanwise planes located at 0, 2.5, 5, 10, 15, 20 and 25 jet diameters downstream of the injector. The NO-PLIF imagery has the advantage of providing snapshots of fluorescence (which is a good analog for injectant mass fraction for limited temperature ranges). This imagery provides detailed information on the normal and lateral spreading characteristics of the ethylene jet.

Hybrid LES/RANS and RANS simulations of normal sonic ethylene injection with an oblique impinging shock downstream of the injector have been performed. The theoretical waves formed by the 5-degree shock generator can be found in Figure 2. As can be seen a pair of shocks and expansion fans emanate from the shock generator. The oblique shock condition formed by the shock generators were imposed by altering the inflow condition to be consistent with the conditions downstream of an oblique shockwave from a five or seven degree shock generator on the top wall as they would be in the experiment. Only the oblique shock is imposed in the numerical investigations and no expansion waves are introduced. The expansion waves would only impact the injection plume downstream of most of the region of interest and it is thought that they would have minimal impact on mixing. The oblique shock from the 5-degree shock generator interacts with the injection plume between the $x/D = 2.5$ and $x/D = 5$ data collection planes and strikes the bottom wall at approximately $x/D = 8.4$. The oblique shock caused by the 7-degree shock generator strikes the bottom wall at approximately $x/D = 5.25$.

RANS simulations for a momentum flux ratio (q) of 1.5 have been performed for
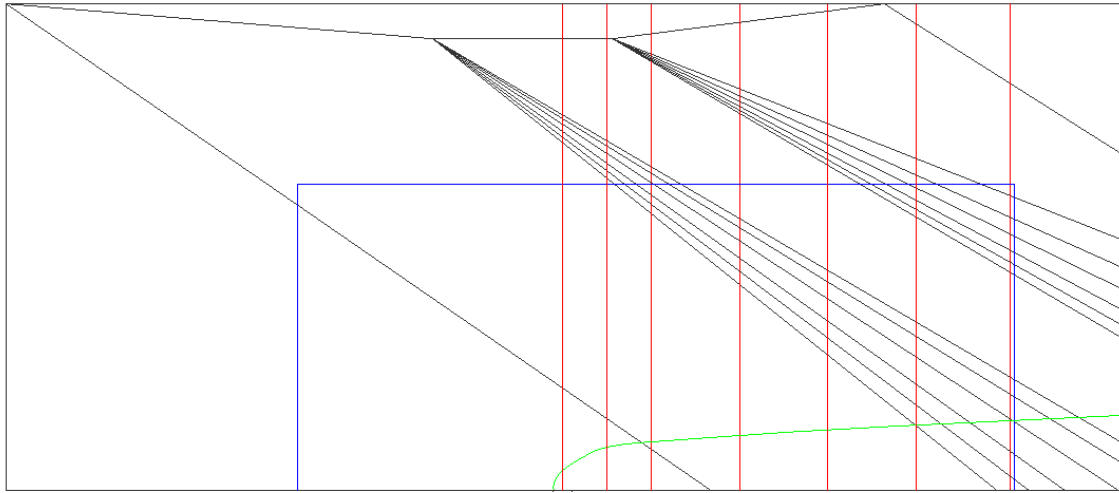
Figure 2: Shocked Injection Analytical Wave Diagram (Interactions Not Shown)

The vertical red lines indicate data planes at which cross-plane NO-PLIF data was gathered experimentally and compared with CFD results in this work. The blue rectangle indicates the computational domain in X and Y.
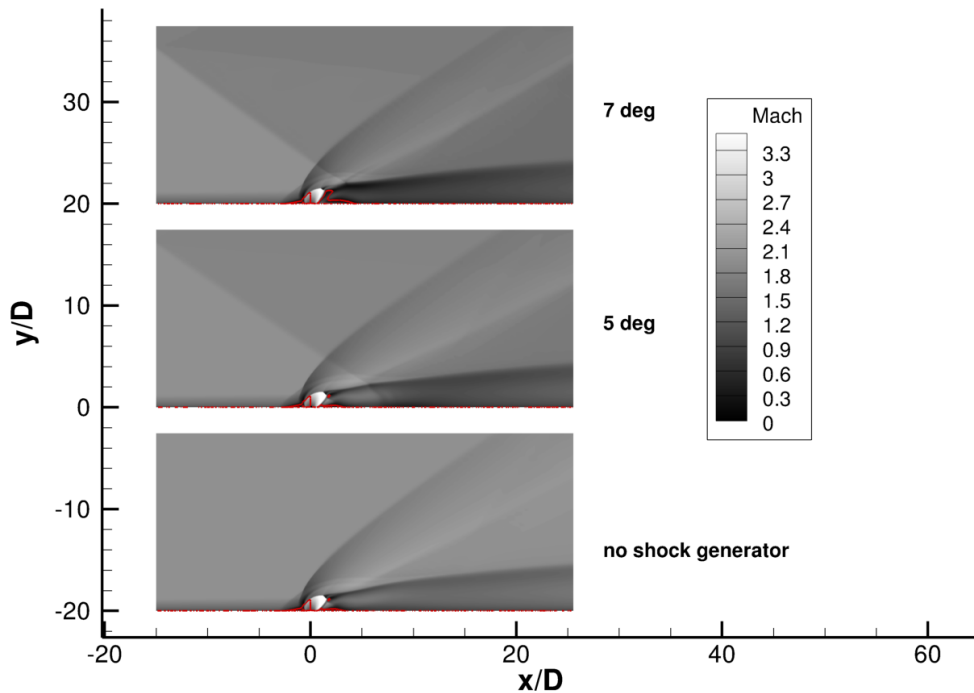
Figure 3: Mach Number Contours for Centerline without Shock Generator and with 5 and 7-Degree Shock Generators Using RANS

Zero axial velocity line shown in red.
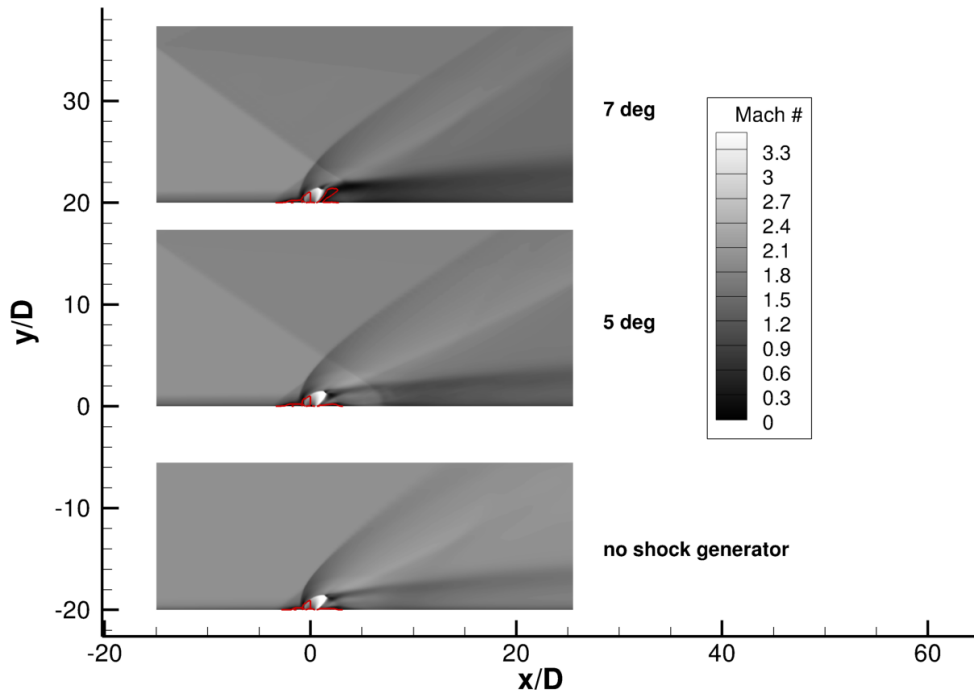
Figure 4: Mach Number Contours for Centerline without Shock Generator and with 5 and 7-Degree Shock Generators Using LES/RANS

Zero axial velocity line shown in red.

injection with no shock generator and then with the 5- and 7-degree shock generator as described above. Center-plane Mach number contours for these simulations can be seen in Figure 3. The red contour line denotes zero axial velocity and implies a significantly larger boundary layer separation for the 7-degree shock generator case than the other two simulations.

Hybrid LES/RANS simulations were performed to better capture the unsteady mixing and the impact of the shock impingement. Time-averaged center-plane contours of Mach number can be seen in Figure 4. The contours look similar to the RANS contours which is consistent with other mixing simulations in that the centerplane flow characteristics are well-predicted by RANS, but off-center characteristics are not. Mixing within the fuel plume shows the biggest advantage of LES/RANS over RANS methods. Figure 5 shows the same plane with crossflow species density contours so that the wave structure as well as the injection plume can be discerned. The sonic line is shown in red and reveals that nearly all of the plume is subsonic in the case with the 7-degree shock generator. This confirms that there is indeed more separation in the 7-degree shock generator case that than the 5-degree case. Since there was limited wind tunnel time, these simulation results were used as evidence that only the 5-degree shock generator should be used, as the 7-degree shock generator introduces too much separation on the bottom wall.
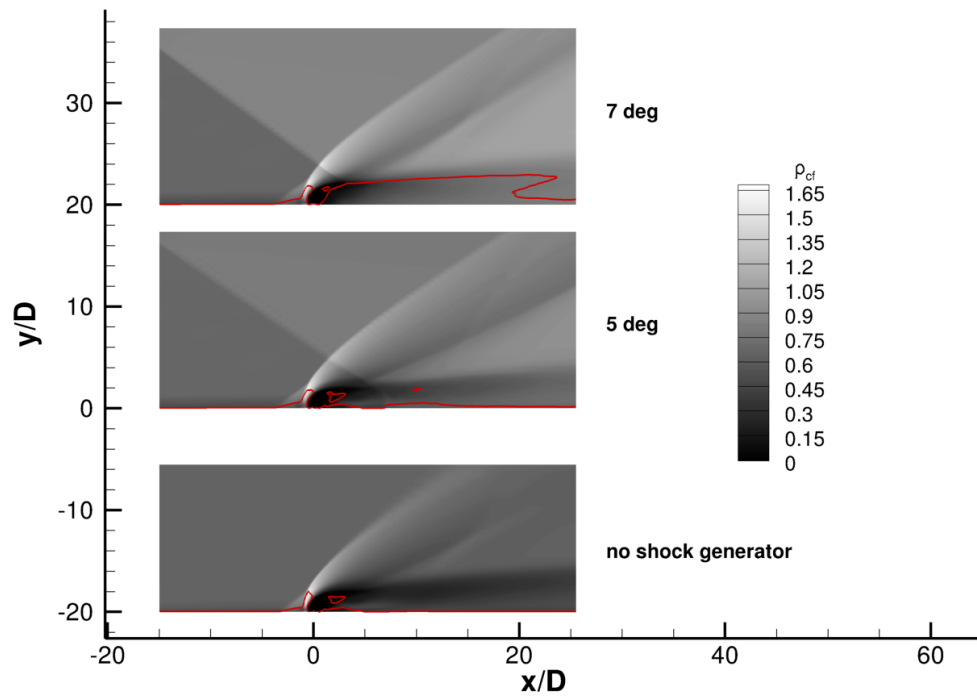
Figure 5: Crossflow Air Species Density Contours for Centerline without Shock Generator and with 5 and 7-Degree Shock Generators Using LES/RANS

Sonic line shown in red.
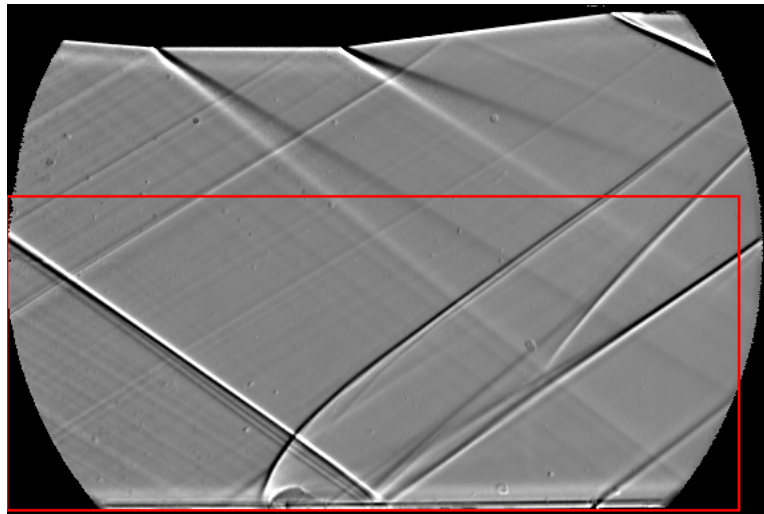
Figure 6: Time-Averaged Experimental Shadowgraph for q=1.5 Air Injection with 5-Degree Shock Generator

X-Y domain for CFD simulations outlined in red.
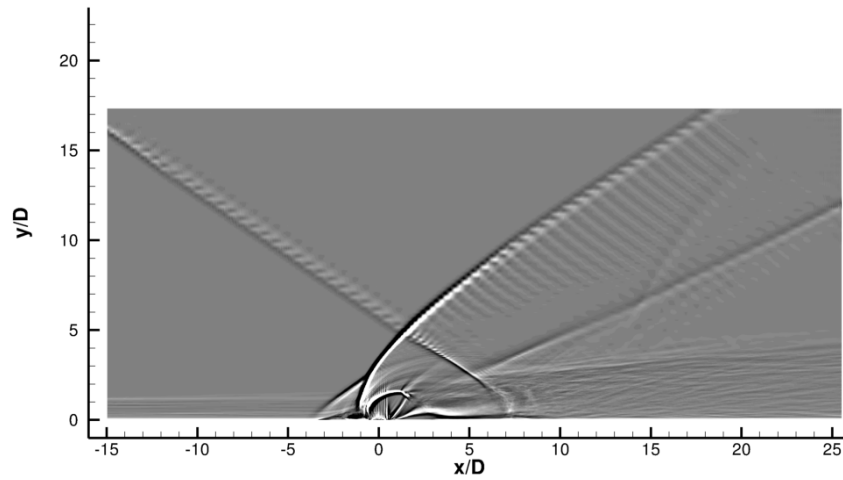
Figure 7: Time-Averaged Numerical Shadowgraph for q=1.5 Ethylene Injection
LES/RANS with 5-Degree Shock Generator
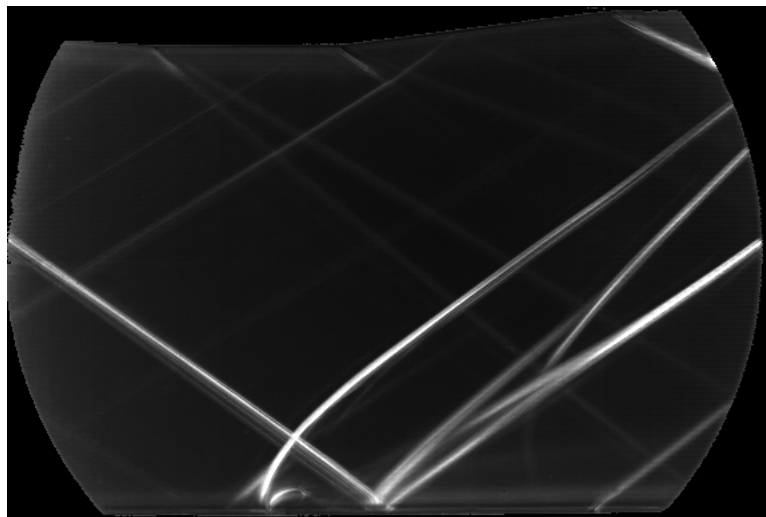
Figure 8: Standard Deviation of Experimental Shadowgraph for q=1.5 Air Injection with
5-Degree Shock Generator

(a) x/D=5 (b) x/D=10 (c) x/D=25
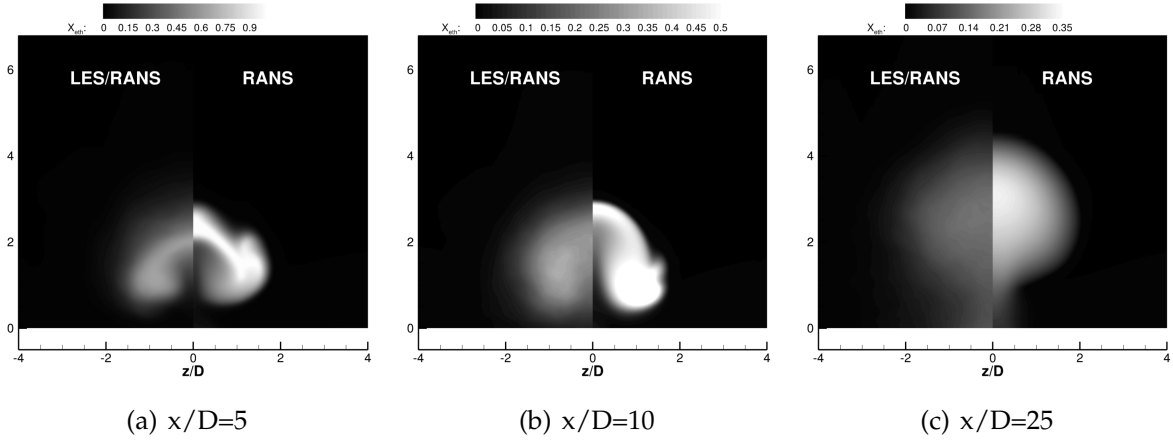
Figure 9: Time-Averaged LES/RANS and RANS Cross Plane Contours of Injectant Mass Fraction for q=1.5, 5-Degree Shock Generator Case

(a) x/D = 5 (b) x/D = 10 (c) x/D = 25
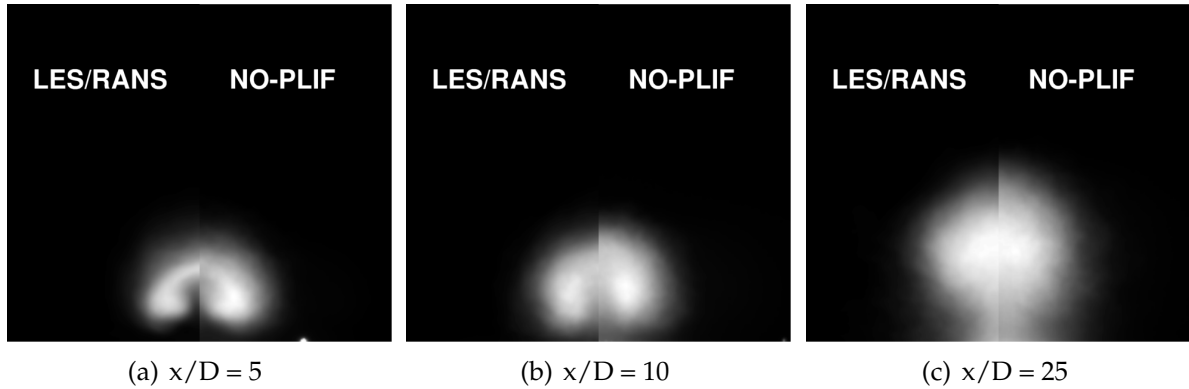
Figure 10: LES/RANS Time-Averaged Cross Plane Contours of Injectant Mass Fraction Compared with NO-PLIF Time Average for 5-Degree Shock Generator Case

Side-view high-speed shadowgraph imagery was collected and the time average of the q = 1.5 case can be seen in Figure 6. Since the 5-degree generator was used in the experiment, the oblique shockwave and expansion wave interact with the injection plume further downstream than in the 7-degree theoretical diagram shown in Figure 2. It is also notable that the upstream expansion wave hardly interacts with the region of interest. The view outlined in red in Figure 6 is recreated numerically in Figure 7 by the LES/RANS simulation. The major flow features are all simulated accurately including the separation and bow shocks upstream of the fuel injection. The experiment shows a shock that is reflected off of the bottom wall that does not appear in the CFD. This appears because the experimental shadowgraph is formed by the density changes across the entire width of the tunnel, whereas the numerical shadowgraph is only determined by the center plane. In the center plane the reflected shock occurs away from the wall because of the injection plume. The experimental standard deviation plot shown in Figure 8 shows that there is not much movement of the shocks involved in the system.

(a) x/D = 5   (b) x/D = 10   (c) x/D = 25
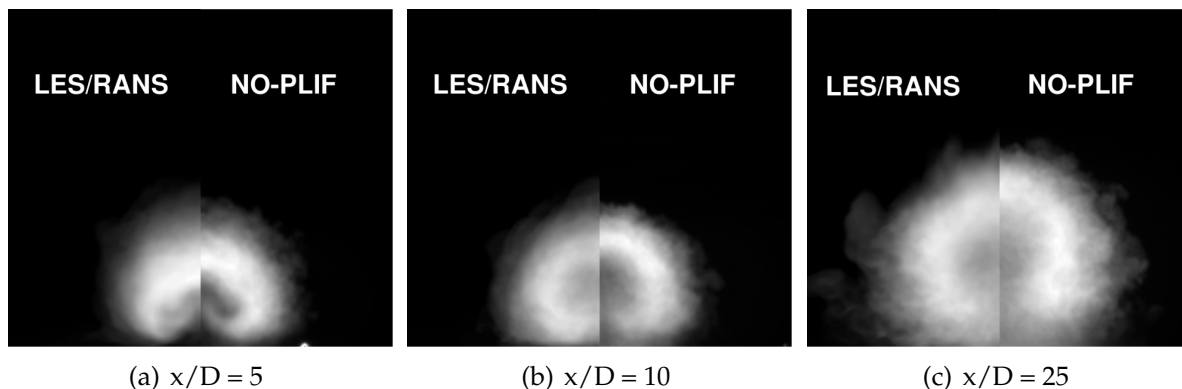
Figure 11: Standard Deviation of LES/RANS Cross Plane Contours of Injectant Mass Fraction Compared with the Standard Deviation of NO-PLIF Imagery for 5-Degree Shock Generator Case

(a) x/D=5   (b) x/D=10   (c) x/D=25
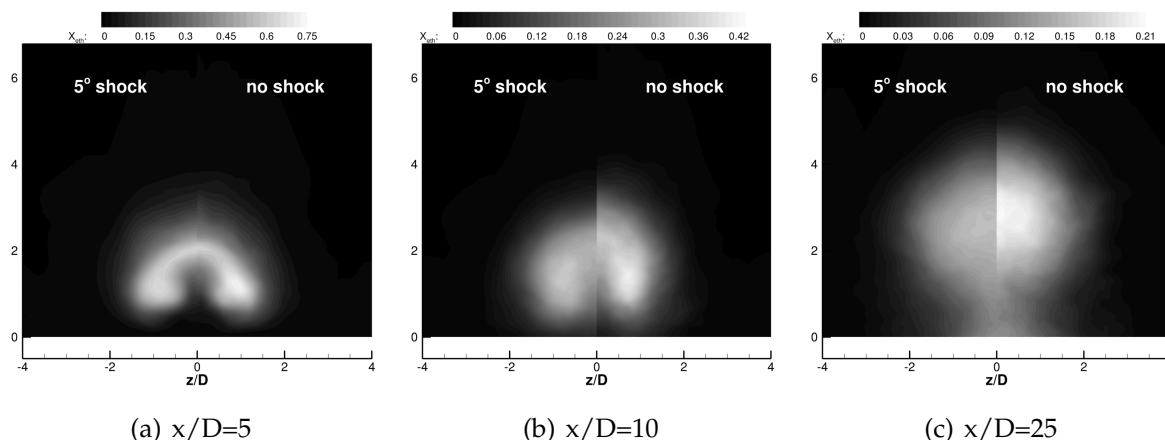
Figure 12: Time-Averaged Cross Plane Contours of Mass Fraction with a 5-Degree Shock Generator and No Shock Generator

Earlier studies [5, 22] have shown that the REACT-MB LES/RANS model is able to capture the shape and mixing within plumes better than RANS simulations. A comparison of RANS to LES/RANS simulations can be seen in Figure 9. The RANS and LES/RANS simulations look strikingly different in their shape and mixing, though the height of the plumes and separation from the bottom wall is similar. The LES/RANS simulation looks very similar to the experimental NO-PLIF imagery seen in Figure 10. The standard deviation imagery seen in Figure 11 again shows that the LES/RANS method did well to simulate the unsteady motion of the plume.

In order to gauge the impact of the shock generator on the mixing of the flow, Figure 12 shows contours of time-averaged injectant mass fraction with and without the 5-degree shock generator using LES/RANS. Downstream of the shock impingement (x/D = 10 and x/D = 25 stations in this case), the injection plume is closer to the wall than the undistorted case. There is also more mixing in the simulation with the shock generator

(a) x/D=5	(b) x/D=10	(c) x/D=25
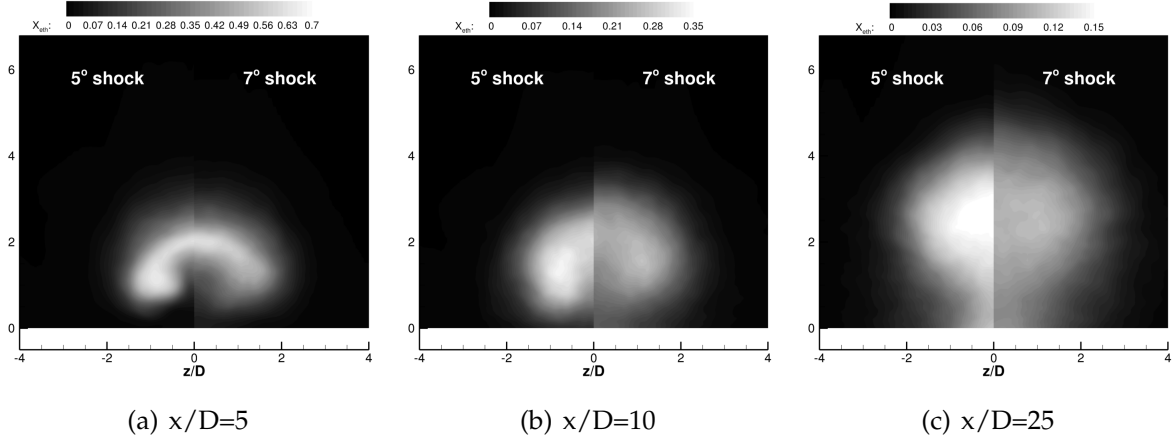
Figure 13: Time-Averaged Cross Plane Contours of Injectant Mass Fraction with 5- and 7-Degree Shock Generator

than without. Both of these impacts are predictable because the flow is slowing down allowing for more time for mixing as well as the pressure increase from the shock is keeping the plume closer to the wall. The simulation of the 7-degree shock generator case is compared to the 5-degree shock generator case in Figure 13. This shows that the 7-degree shock generator causes substantially more mixing than the 5-degree case. This falls in line with the reasoning that a stronger shock slows the flow down more allowing for more mixing. However, the plume itself is further from the wall than the 5-degree case even though the pressure jump from oblique shock would be greater for the 7-degree shock generator. It is theorized that this is due to the large separation seen in Figures 4 and 5.

In order to better quantify the impact of the shock generators on mixing, the mixedness parameter as defined by Fric [23] has been calculated for the LES/RANS simulations:

$$M = 1 - \frac{\left[\int |c - \bar{c}|\, dA\right]}{\left[\int |c - \bar{c}|\, dA\right]_{x/D=0}} \tag{1}$$

where c is time-averaged mixture fraction and $\bar{c}$ is the mixture fraction averaged over a given plane for the time-averaged solution. This method was also applied to the intensity values from the averaged NO-PLIF imagery for the 5 degree shocked and unshocked case for q = 1.5. The mixedness parameter for the experimental and computational data are compared in Figure 14. It can be seen from this plot that while there is a fairly large shift in mixedness between the case with no shock generator and the one with a 5-degree shock generator, there is not much of an increase in mixedness when the 7-degree generator is used. But, when the 7-degree shock generator is used, a large drop in total pressure is seen – illustrating the downside of using shocks to increase mixing within a scramjet.
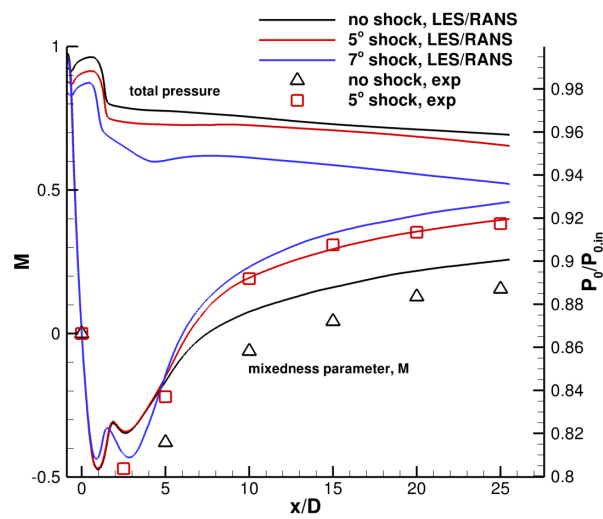
Figure 14: Time-Averaged and Experimental Mixedness Parameter and Computational Total Pressure Losses Averaged Over Each Streamwise Plane

4.2 Shocked Cavity

Cavities are often used to provide a stable flame for supersonic combustion by inducing separation within [12,13]. The presence of a cavity downstream of a flush wall injector increases flow residence time, allowing for greater time for mixing and combustion. Steady-state numerical investigations of cavity flameholders have been performed regularly in the past using steady-state methods [14,15] but only in recent years have computational resources allowed for the simulation of these flows with unsteady LES and LES/RANS methods. In addition, the impact of flow distortion caused by oblique shocks from the cowl in scramjet flowpaths is of interest. This section discusses the impact of an oblique shock impinging in the region of a cavity flameholder. For mixing flows, computational studies were performed with both RANS and hybrid LES/RANS, while only RANS was used for combusting flows.

An experimental investigation of the impact of oblique shock waves on fuel injection in the cavity region was conducted to complement the computational studies being performed [24]. A single flush wall injector was located in the bottom wall of the tunnel a half inch upstream of the ramped cavity, with a 2.5° divergence starting upstream of the injector and cavity as seen in Figure 15. The 2 by 6 inches, Mach 3 configuration of Research Cell 19 (RC19) at the Air Force Research Laboratory Facility [25] was used. For these mixing flows, the total temperature and pressure were approximately 300K and 1.2 MPa, respectively. On the upper wall, a shock generator wedge was mounted as seen in Figure 15, and could be translated axially. The shock generator could be traversed three inches axially, which allowed the study of multiple shock impingement locations, from upstream of the injector to the middle of the cavity region. Three wedges seen in Figure 16 were fabricated and two wedges were tested, with deflections of 6.1° and 7.7° (the 5° wedge was not used due to irregularities in fabrication). The simulations focused on the 7.7° wedge.

Numerous diagnostics were used during the experiments. A shadowgraph system was used to calibrate the positioning of the shock generator as well as record the basic shock structures of the different configurations. For the non-combusting runs, NO-PLIF was used to record snapshots of injectant along spanwise planes. This imagery provided detailed information on the normal and lateral spreading characteristics of the non-reacting air jet. Ice crystal illumination using Mie scattering techniques were recorded as well for the low temperature cases. These measurements provide snapshots that are similar to crossflow temperature measurements and can be used as another way of visualizing the flow field shock structures. These proved important in the 7.7° wedge case because no shadowgraph imagery was performed for that wedge.

4.2.1 Cold Flow Cases

Flow Structures

In order to better understand the flow features of the cavity flameholder, it is first instructive to examine the flow structures far off-center in this flow outside of the
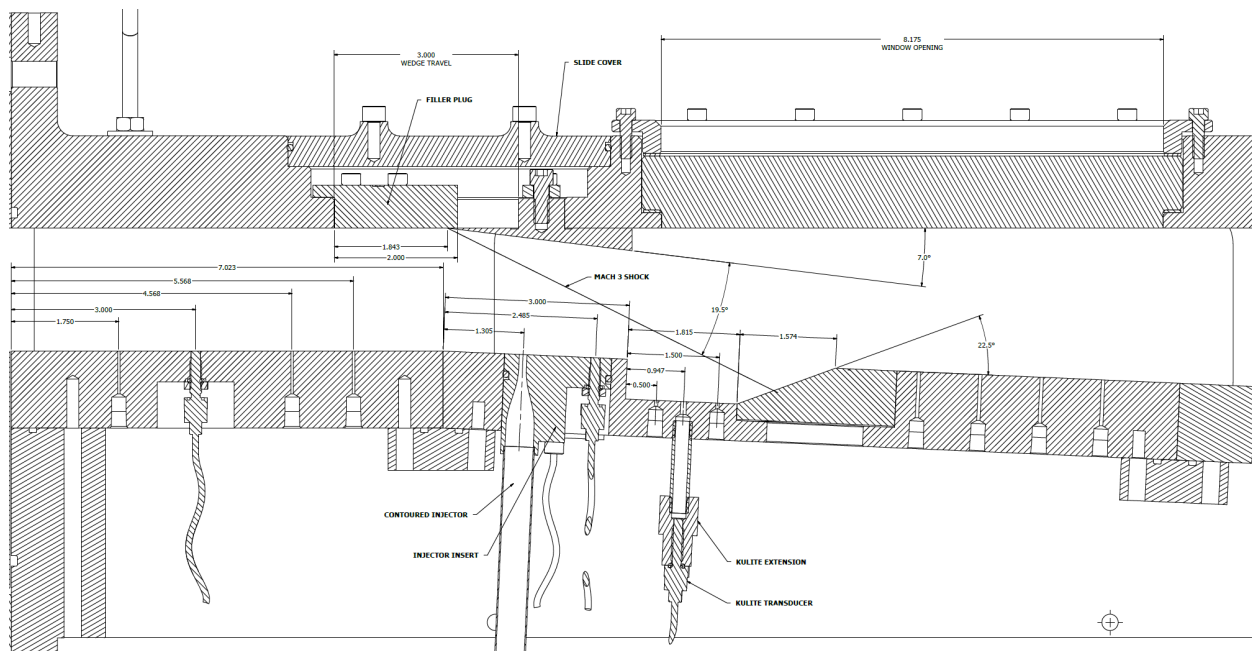
Figure 15: Schematic for Experiment with 7° Shock Generator in the Shock-On-Cavity Position

Units are inches. Injector block is reversed in the present experiment such that the injector is 0.5 inches upstream of the cavity.

influence of injection. To identify the different shock waves for each of the three cases, contours of static pressure seen in Figure 17 are analyzed to make a simplified wave diagram for the waves relevant to the cavity mixing (Figure 18). Figure 19 shows the Mach contours at this location.

There are three main types of shocks seen in the flow field away from the injector. The shock labelled S1 is the shock formed by the shock generator. The shock labelled S2 is formed by the separation of the boundary layer just upstream of the cavity. This phenomenon can be seen more clearly in the Mach contours in Figure 19. The No-Shock case doesn't show a separation upstream of the cavity thus S2 isn't present for that case. For the Shock-On-Jet case, there is a small shock-induced separation which causes a shallow, weak S2 shock that is also slightly turned by the expansion fan. For the Shock-On-Cavity case, the shock hits in the middle of the cavity and causes a larger separation upstream of the cavity causing a steeper and stronger S2 shock. The S3 shock is what is often referred to as a cavity close-out shock. It is caused by the turning of the flow caused by the ramp at the downstream end of the cavity. For the No-Shock case this is a straightforward interaction with a S3 shock formed that corresponds to the small blockage formed by the cavity closeout and its associated turning of the flow. For the Shock-On-Jet case the S3 shock is more severe than the others because the turning angle is more sharp than the other two cases. This is because S1 in this case causes the shear layer to be pushed towards the bottom wall, thus making the flow make a more severe turn at the cavity closeout. It is also clear that the expansion fan turns S2 and S3 slightly
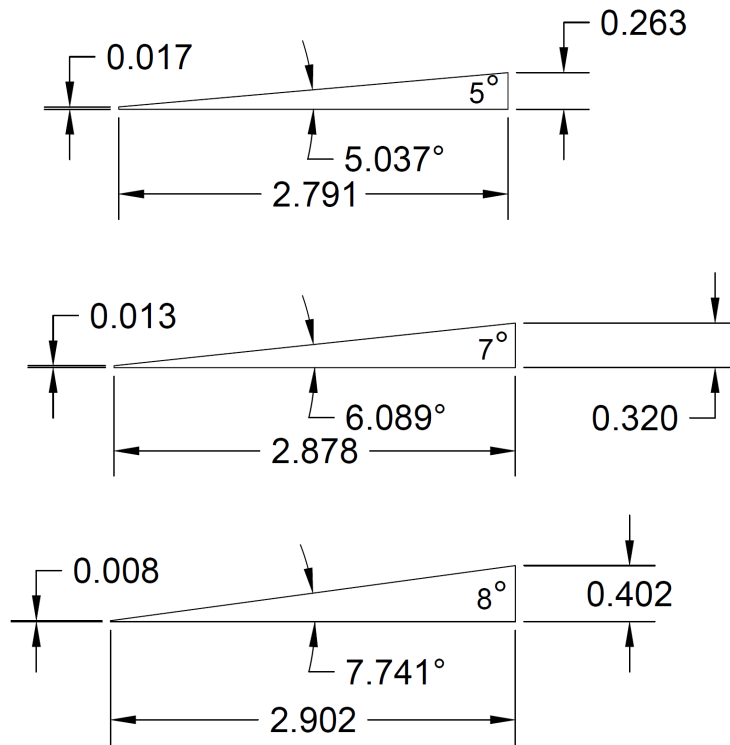
Figure 16: As-Built Wedge Shock Generators

Measurements all shown in inches. Nominal design wedge angles were 5, 7 and 8 Degrees.
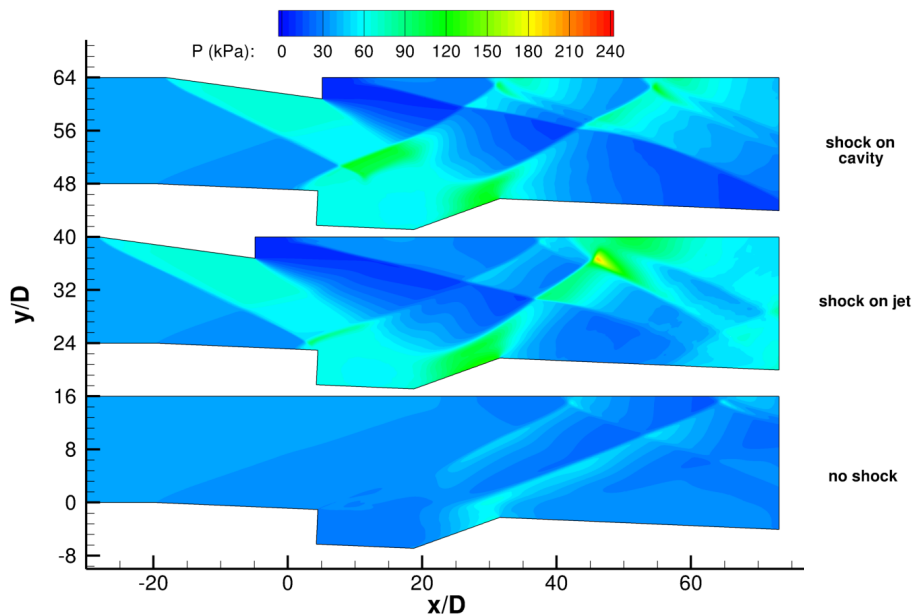
Figure 17: Contours of Time-Averaged Static Pressure at z/D = -11.9
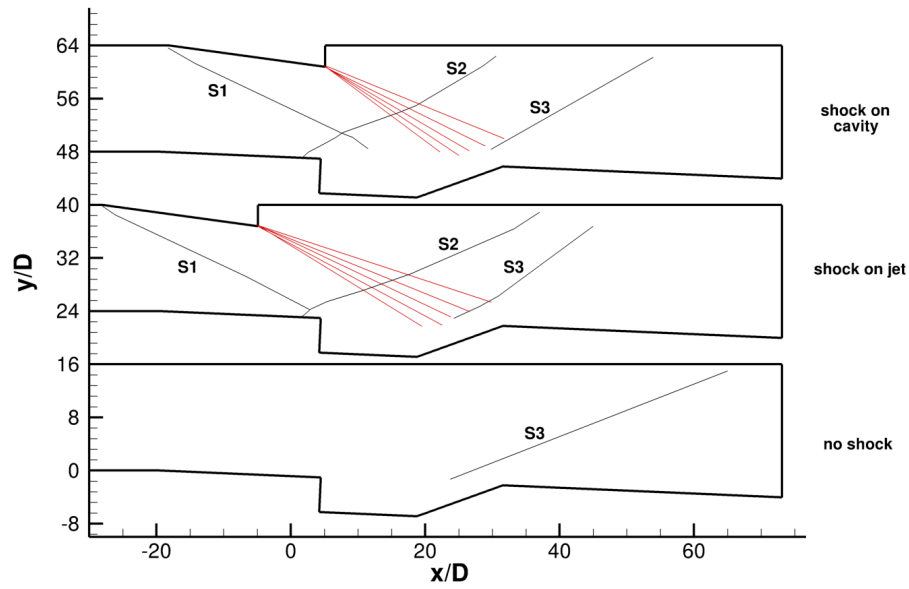
Figure 18: Wave Patterns Important to Cavity Mixing

Shocks in black, expansion fan in red.
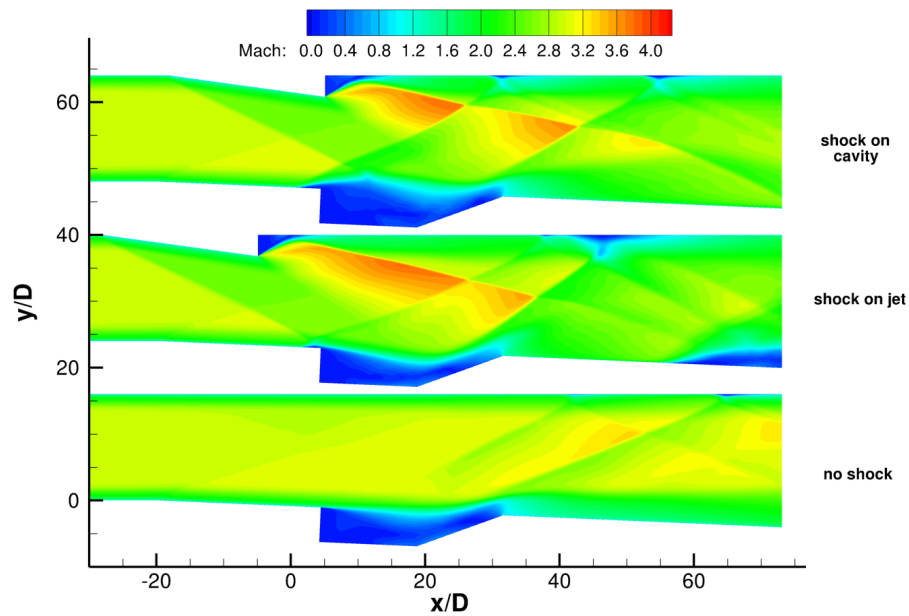
Figure 19: Contours of Time-Averaged Mach Number at z/D = -11.9
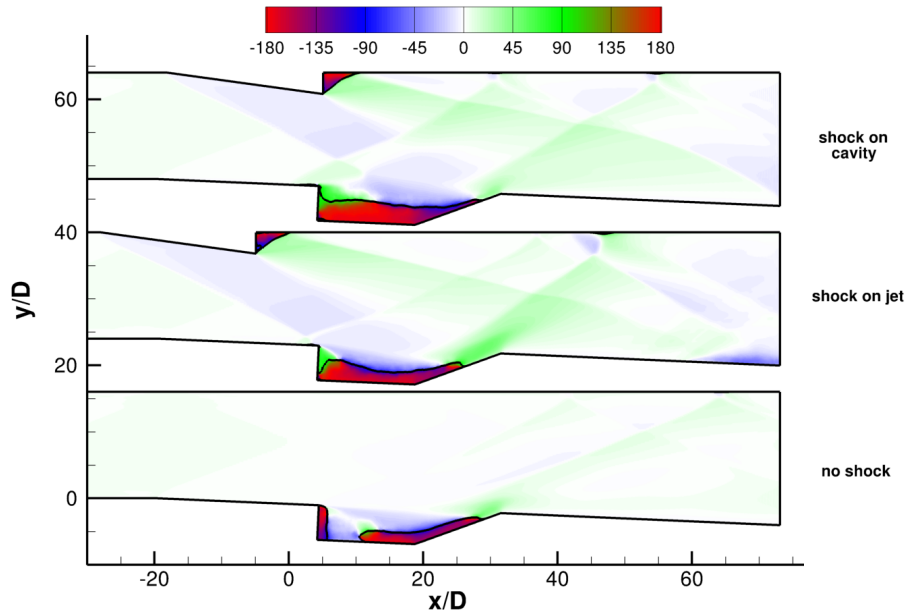
Figure 20: Flow Angle Relative to Bottom Wall from Time-Averaged LES/RANS
Simulation at z/D = -11.9

*White denotes flow from left to right, red denotes flow from right to left, green denotes upward flow, and
blue denotes downward flow. Black contour line denotes zero axial velocity.*

where they interact.

A contour plot of flow angle in a plane far from the centerplane (measured relative to the
2.5° divergence angle of the bottom wall) can be seen in Figure 20 with the black line
indicating the zero velocity parallel to the bottom wall (i.e. the edge of the reversed flow
zone). The center of rotation can be gleaned from the point around which the full
spectrum of the contour levels is present, for instance at $x/D = 13$ and $y/D = -5$ in the
No-Shock case in Figure 20. From these plots you can infer that the reversed flow zone in
the No-Shock case extends from approximately $x/D = 10$ to the end of the cavity and
the flow rotation is centered at about $x/D = 13$. In the Shock-On-Jet case the reversed
flow zone is more upstream and the flow rotation is centered at about $x/D = 8$. For the
Shock-On-Cavity case the reversed flow zone extends the length of the cavity and the
flow rotation is centered at about $x/D = 13$.

With the knowledge of the off-center flow structures, the center plane flow structures
with injection is easier to understand. Injection upstream of the cavity introduces a bow
shock S4 as shown in Figures 22 – 21. In order to confirm that these shocks were correctly
simulated, center plane temperature contours are compared with the ice crystal Mie
scattering in Figures 23–25. The shape of the slower (and warmer) cavity flow is
well-predicted for each case.

The flow angle contours for the center plane can be seen in Figure 26. They are much
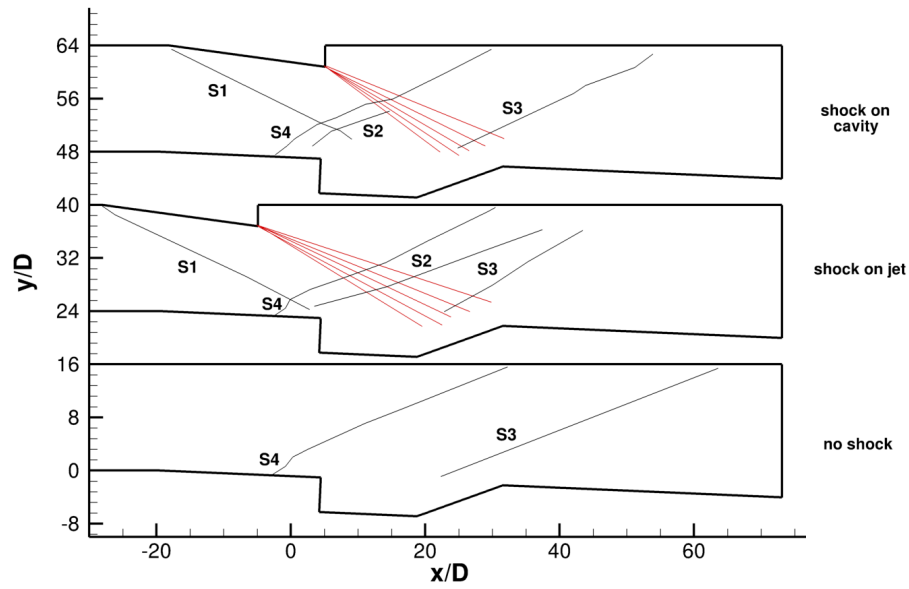
Figure 21: Wave Patterns Important to Cavity Mixing at Center Plane

Shocks in black, expansion fan in red.
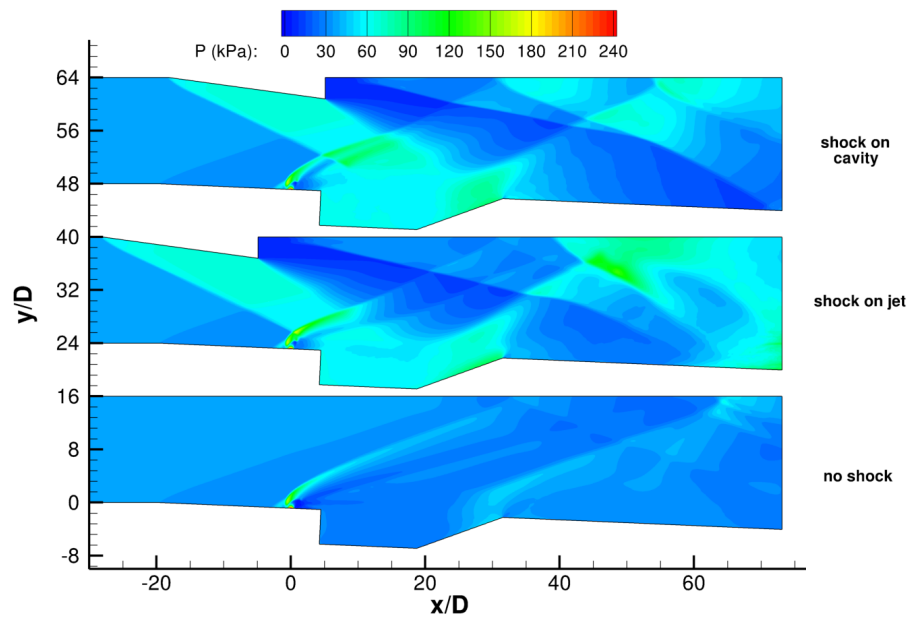
Figure 22: Contours of Time-Averaged Static Pressure at Center Plane

(a) Experimental Mie Scattering   (b) LES/RANS Temperature
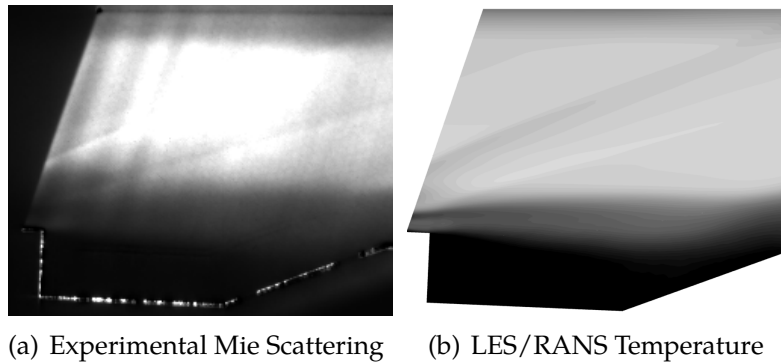
Figure 23: Time-Averaged Experimental Mie Scattering Ice Crystal and LES/RANS contours of Temperature for No-Shock Case at Center Plane

(a) Experimental Mie Scattering   (b) LES/RANS temperature
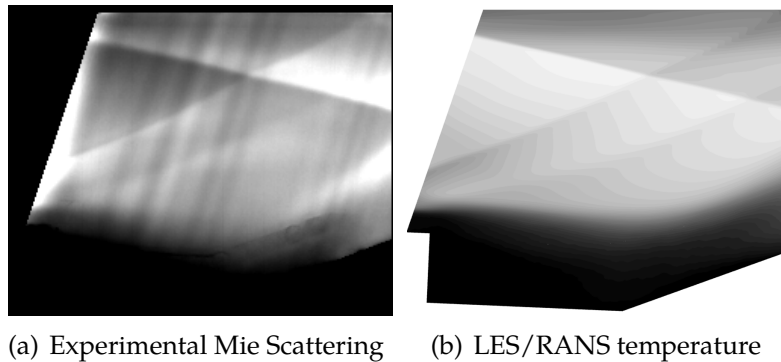
Figure 24: Time-Averaged Experimental Mie Scattering Ice Crystal and LES/RANS Contours of Temperature for Shock-On-Jet Case at Center Plane

(a) Experimental Mie scattering   (b) LES/RANS temperature
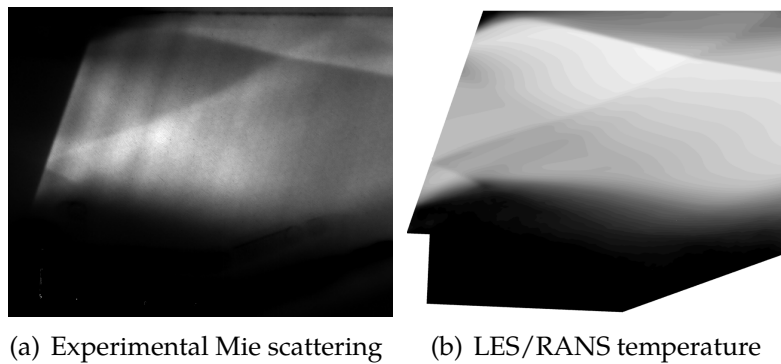
Figure 25: Time-averaged experimental Mie Scattering Ice Crystal and LES/RANS Contours of Temperature for Shock-On-Cavity Case at Center Plane
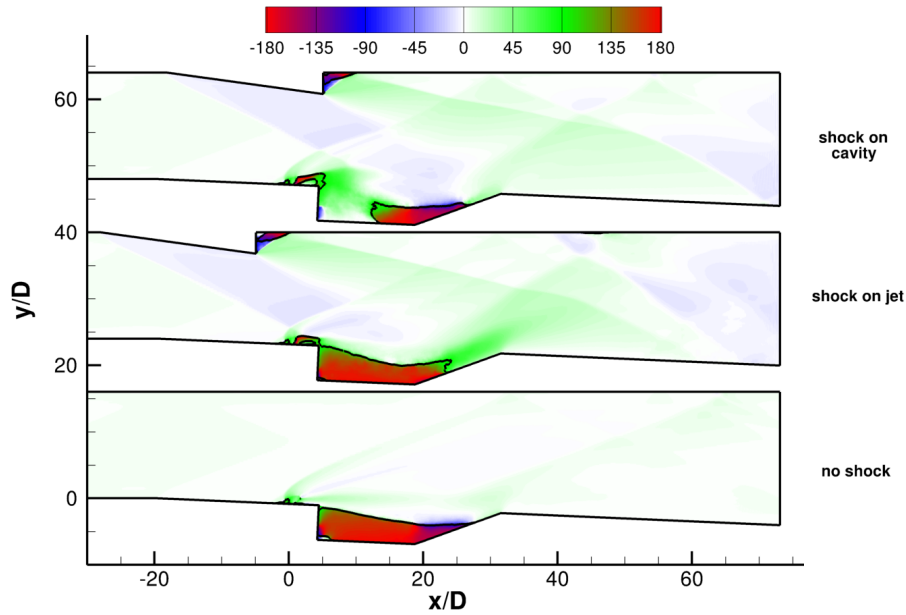
Figure 26: Flow Angle Relative to Bottom Wall from Time-Averaged LES/RANS
Simulation at z/D = 0

*White denotes flow from left to right, red denotes flow from right to left, green denotes upward flow, and
blue denotes downward flow. Black contour line denotes zero velocity parallel to divergent bottom wall.*

different than the flow angle contours in Figure 20. Specifically, the reversed flow section
for the Shock-On-Cavity case is isolated to the cavity closeout ramp and the wake region
of the jet. Also, the reversed flow region for the other two cases is larger on the
centerplane than it was off-center. In order to better understand these phenomena, 3D
iso-surfaces of the reversed flow boundary can be seen in Figures 27-29 as well as 3D
injectant mass fraction iso-surfaces for each case.

The No-Shock iso-surface in Figure 27(a) shows a very small reversed flow region in the
jet's wake. Also the plume itself carves out an un-reversed flow section in the middle of
the cavity. The plume in Figure 27(b) shows no deflection toward the bottom wall and
little lateral spreading of the injection in the cavity. The iso-surfaces for the Shock-On-Jet
case in Figure 28(a) reveal two un-reversed flow regions on either side of the injectant
plume at the upstream end of the cavity. In Figure 28(b), the plume is deflected toward
the bottom wall due to the upstream oblique shock and the injectant on the bottom wall
has moved further upstream than the No-Shock case. The Shock-On-Cavity case has an
un-reversed flow section in the middle of the cavity just below the plumein Figure 29(a).
As a result, the plume seen in Figure 29(b) does not move much upstream, but is instead
pushed laterally away from the un-reversed flow section.

A comparison of the time-averaged Mach number on the centerplane is shown in Figure
30. This image more clearly shows the impact of the shock structure on the shear layer

(a) Reversed flow

(b) $X_{inj} = 0.04$
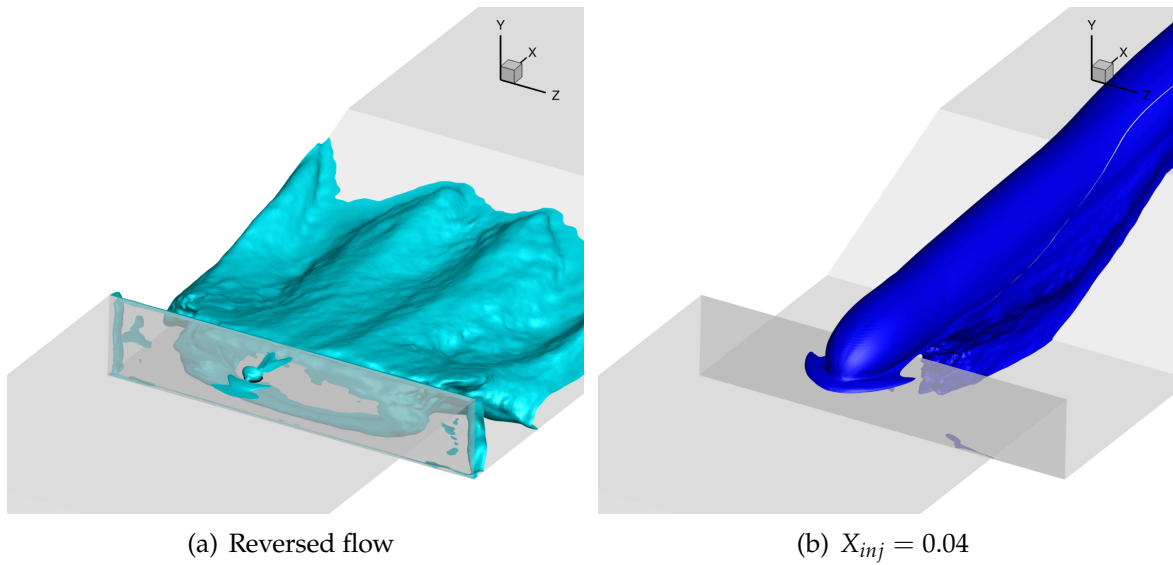
Figure 27: 3D Iso-Surfaces for 'No-Shock' Case

(a) Reversed Flow

(b) $X_{inj} = 0.04$
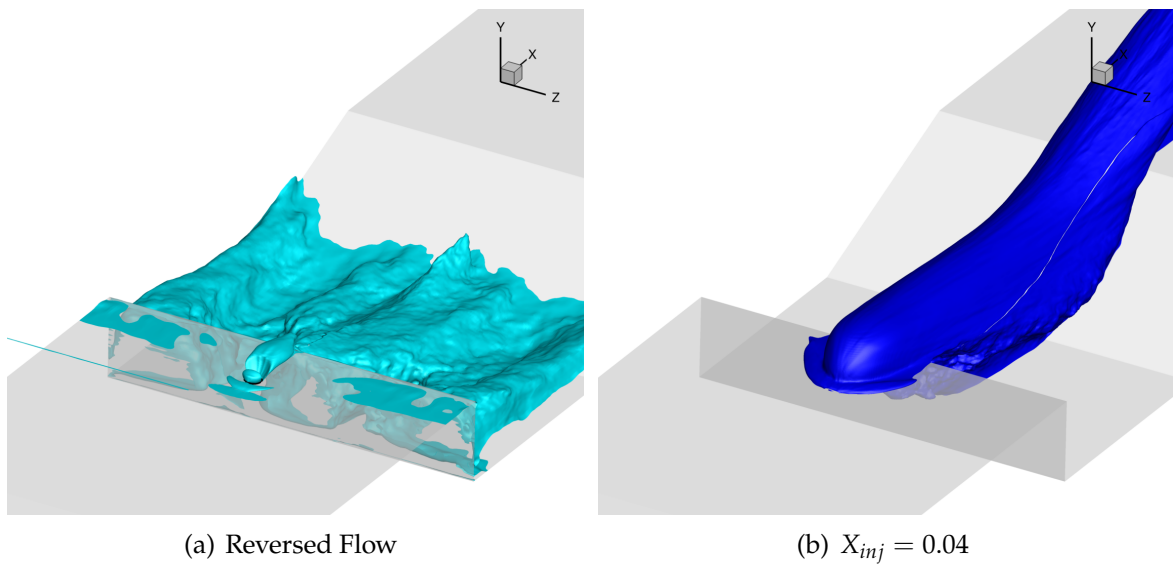
Figure 28: 3D Iso-Surfaces for Shock-On-Jet Case

(a) Reversed Flow (b) $X_{inj} = 0.04$
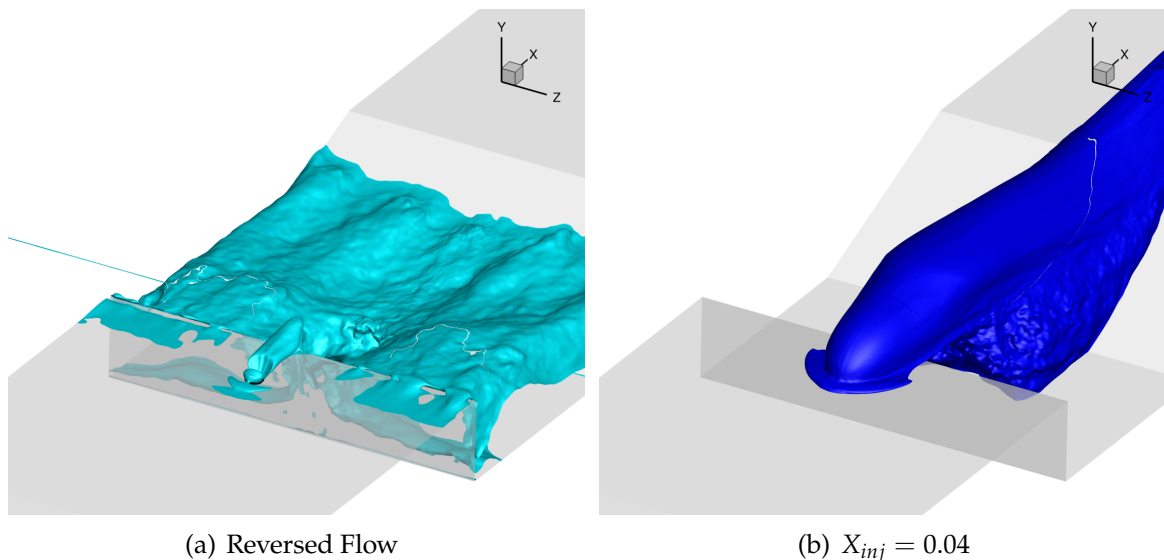
Figure 29: 3D Iso-Surfaces for Shock-On-Cavity Case

over the cavity.

Mixing

The flow structures resulting from S1 and its position strongly impact the mixing downstream. Figure 31 shows the idealized wave diagram overlaid with injectant mass fraction. From this you can see that the unshocked case is the least mixed at the center plane. For the two shocked cases, they exhibit different patterns of mixing. The Shock-On-Jet case shows an injection plume that initially turns down towards the bottom wall but then sharply turns away from the bottom wall after crossing through the expansion fan and S3. The Shock-On-Cavity case sees the plume rise from the bottom wall initially because of the large cavity recirculation zone caused by the impinging shock. Downstream of S1 the plume starts to move towards the bottom wall and then turns away from the bottom wall as it proceeds through the expansion fan and S3, but not as much as the Shock-On-Jet case. The behavior of these plumes in the LES/RANS simulation was also observed in the NO-PLIF experimental imagery seen in Figures 32–34.

Figure 35 shows the same idealized wave structures as Figure 31 on top of an instantaneous injectant mass fraction distribution as predicted by the LES/RANS simulations. In addition to mean information, NO-PLIF experimental also provides information on the instaneous plume shape in a given plane. Figures 36–38 show center plane NO-PLIF images compared with instantaneous injectant mass fraction for the LES/RANS simulations. As with all the NO-PLIF comparisons, they are qualitative in nature as the brightness and contrast is adjusted for each image. The plume structures in the No-Shock case are the least diffuse in the simulation as well as the experimental images. Also the Shock-On-Cavity simulation shows the most diffuse plume with the
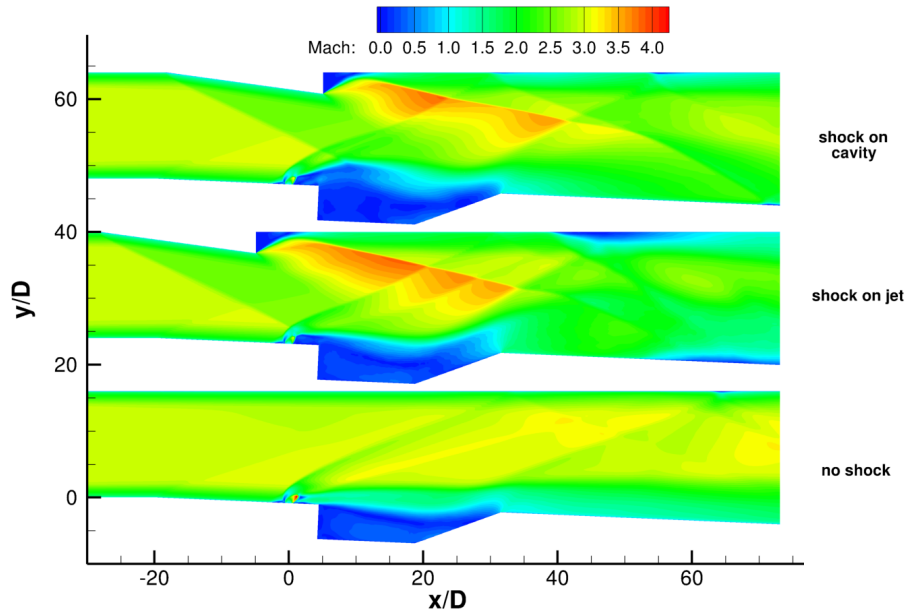
Figure 30: Center Plane Contours of Time-Averaged Mach Number
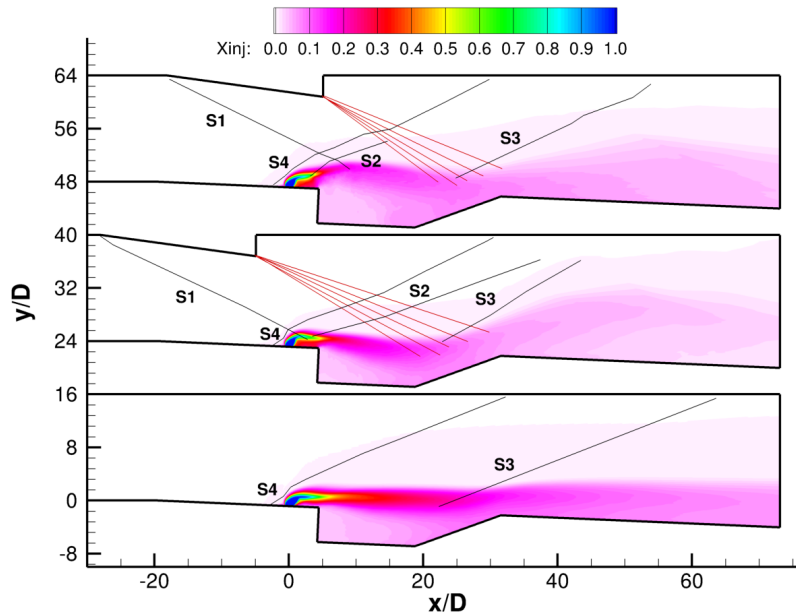
Figure 31: Time-Averaged Injectant Mass Fraction Contours with Idealized Wave Structures

(a) Experimental NO-PLIF   (b) LES/RANS Injectant Mass Fraction
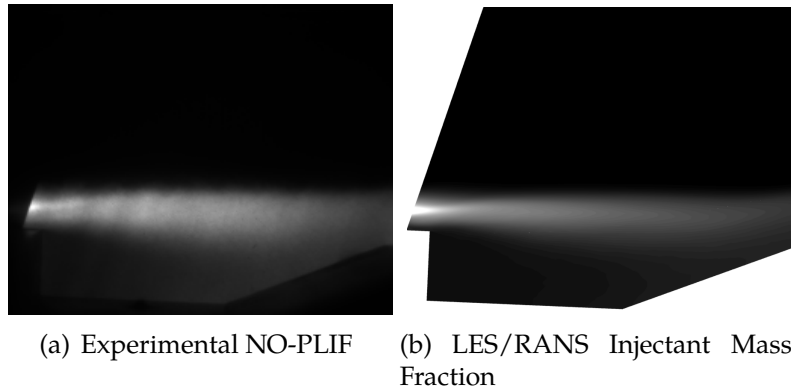
Figure 32: Time-Averaged Experimental NO-PLIF Imagery and LES/RANS Contours of Injectant Mass Fraction for No-Shock Case at Center Plane

(a) Experimental NO-PLIF   (b) LES/RANS Injectant Mass Fraction
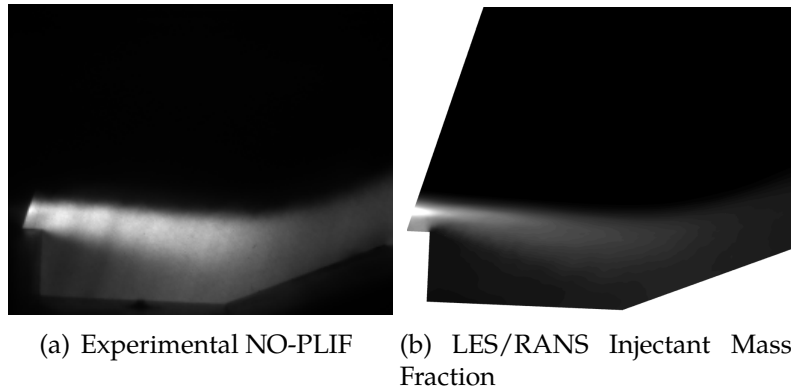
Figure 33: Time-Averaged Experimental NO-PLIF Imagery and LES/RANS Contours of Injectant Mass Fraction for Shock-On-Jet Case at Center Plane

(a) Experimental NO-PLIF   (b) LES/RANS Injectant Mass Fraction
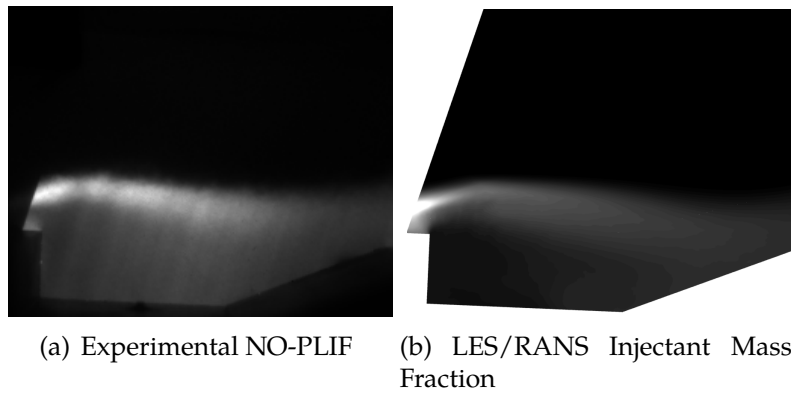
Figure 34: Time-Averaged Experimental NO-PLIF Imagery and LES/RANS Contours of Injectant Mass Fraction for Shock-On-Cavity Case at Center Plane
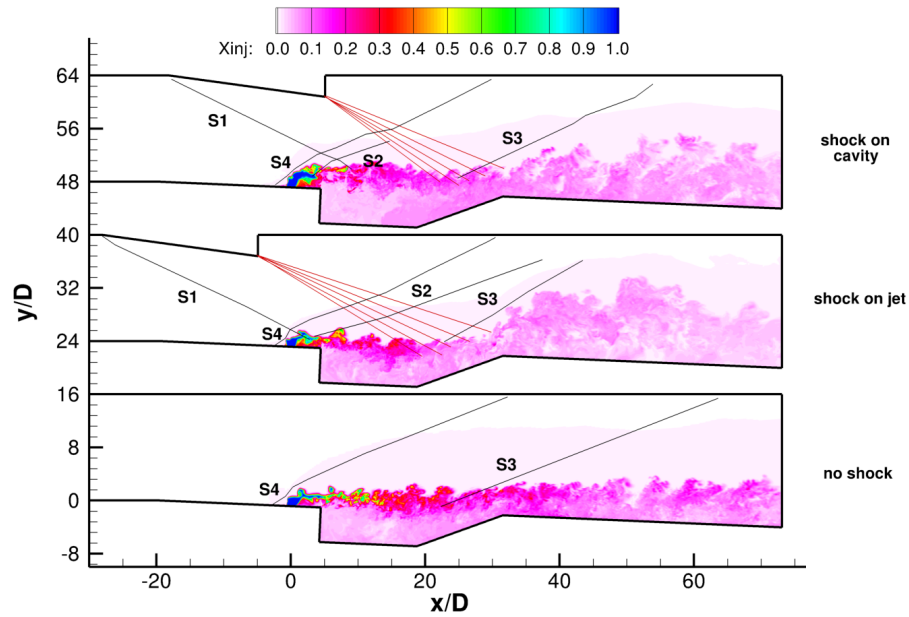
Figure 35: Center Plane Contours of Instantaneous Injectant Mass Fraction

(a) Experimental NO-PLIF

(b) LES/RANS Injectant Mass Fraction
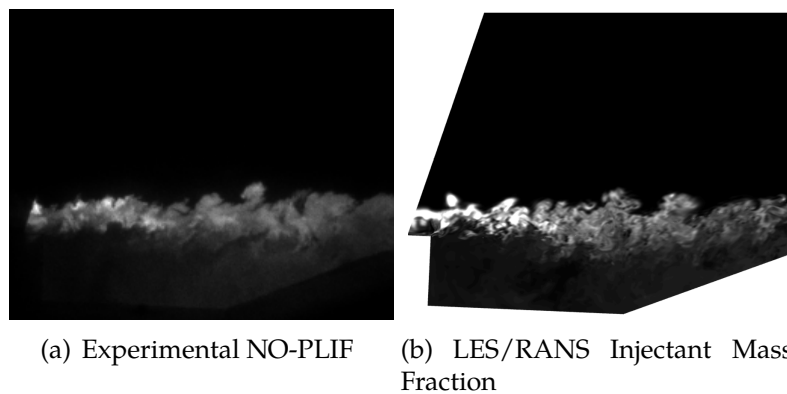
Figure 36: Snapshots of Experimental NO-PLIF Imagery and LES/RANS Contours of Injectant Mass Fraction for No-Shock Case at Center Plane

(a) Experimental NO-PLIF

(b) LES/RANS Injectant Mass Fraction
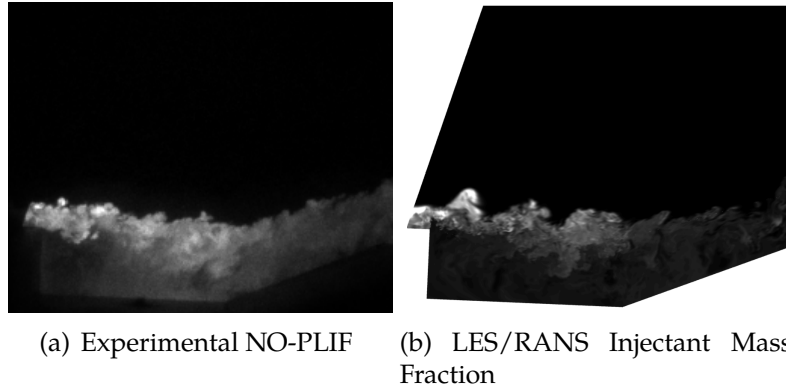
Figure 37: Snapshots of Experimental NO-PLIF Imagery and LES/RANS Contours of Injectant Mass Fraction for Shock-On-Jet Case at Center Plane

(a) Experimental NO-PLIF

(b) LES/RANS Injectant Mass Fraction
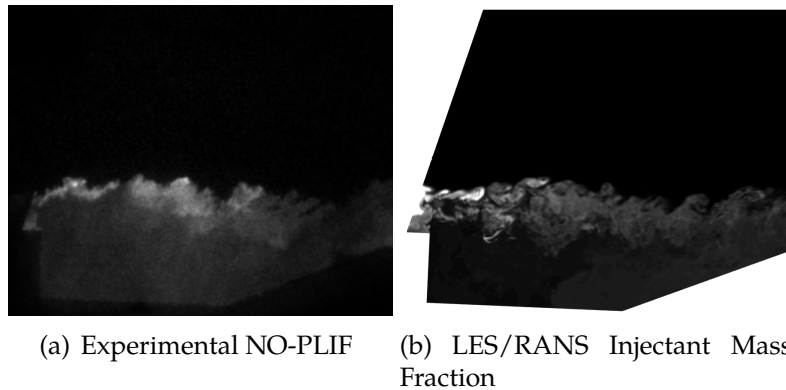
Figure 38: Snapshots of Experimental NO-PLIF Imagery and LES/RANS Contours of Injectant Mass Fraction for Shock-On-Cavity Case at Center Plane
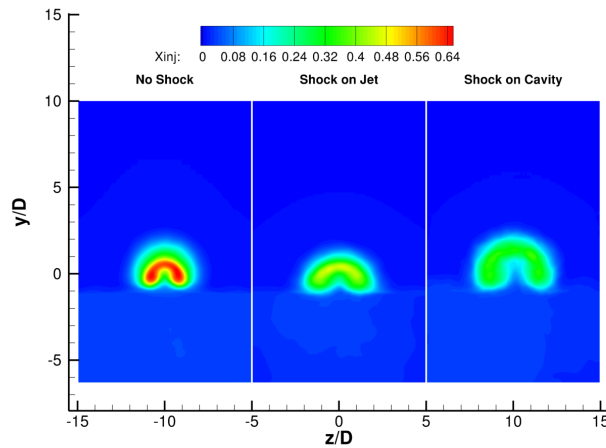
Figure 39: Time-Averaged LES/RANS Contours of Injectant Mass Fraction for q=1, x/D = 5

least defined plume structures.

Slices at constant axial locations in Figures 39–41 show the differences in mixing off-center. The most basic observation is that the shocked cases mix much more fully than the unshocked case. Also, the Shock-On-Cavity case shows more lateral spreading in the cavity than the other two cases. Note that these images only show about half the computational domain width. Also at the first station in Figure 39, it is notable that the lower bound of the counter-rotating vortices line up along shear layer for all three cases, but the shape and mixing of these vortices varies widely between the three. The top of the counter-rotating vortex pair for the Shock-On-Cavity case is lifted substantially and there is a distinct spatial separation between the vortex pair at the center. The vertical penetration is increased due to the the outward displacement of the shear layer seen in Figure 30.

4.2.2 Reacting Flow Cases

CFD++ RANS simulations

The outline of the solution domain is shown in Figure 42 and represents a half-width of the RC19 flowpath, with the symmetry plane shaded in blue. The domain includes the Mach 3.0 facility nozzle. The overall length of flowpath is 45 inches, and has a 2 by 6 inches cross-section at the end of the nozzle, but with the symmetry assumption only 3 inches of the width are simulated . Table 1 shows a summary of the numerics that were used in this analysis.

On the centerline is the primary (jet) injector which is upstream of the cavity and one of the cavity injectors. There are a total of eleven cavity injectors in the full-width, spaced in half inch increments. Five full injectors and one half injector are included in the
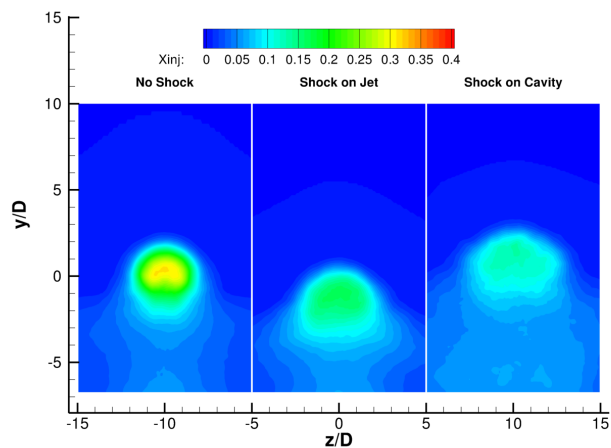
Figure 40: Time-Averaged LES/RANS Contours of Injectant Mass Fraction for q=1, x/D = 15
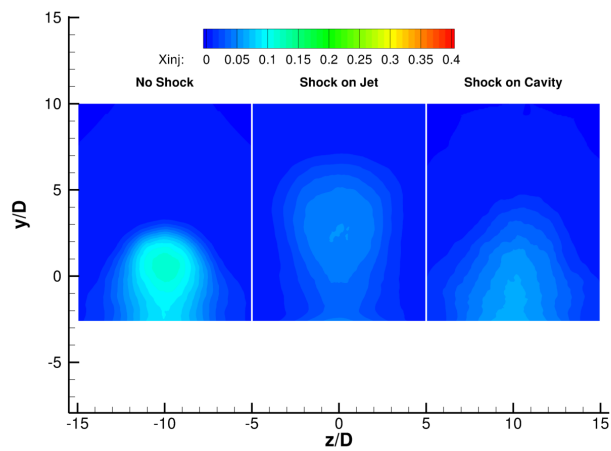
Figure 41: Time-Averaged LES/RANS Contours of Injectant Mass Fraction for q=1, x/D = 40
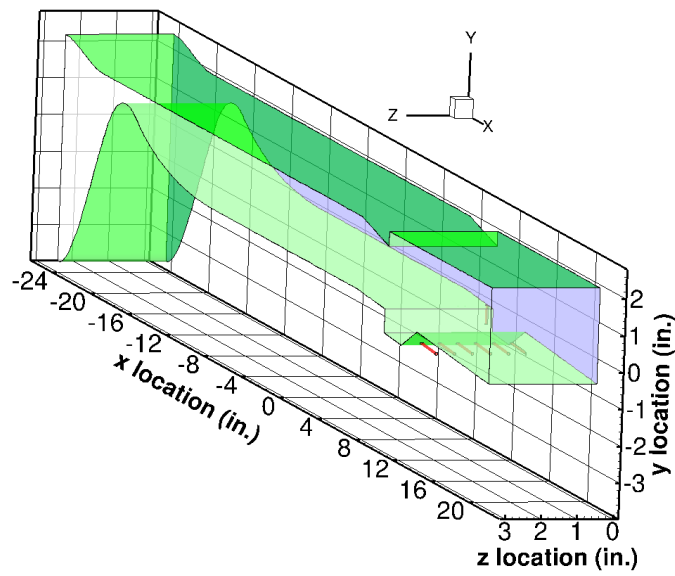
Figure 42: Outline of Cavity Flowpath Half-Geometry
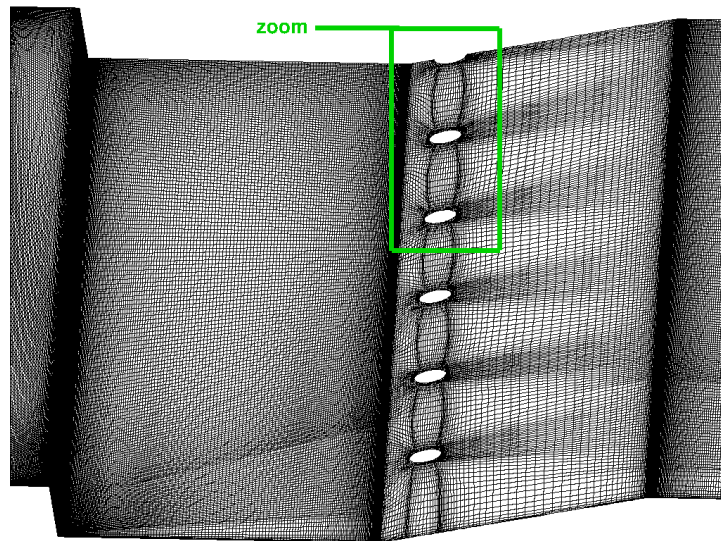
Figure 43: Cavity Bottom-Wall Grid Topology Showing Cavity Injectors (CFD++ RANS simulations)
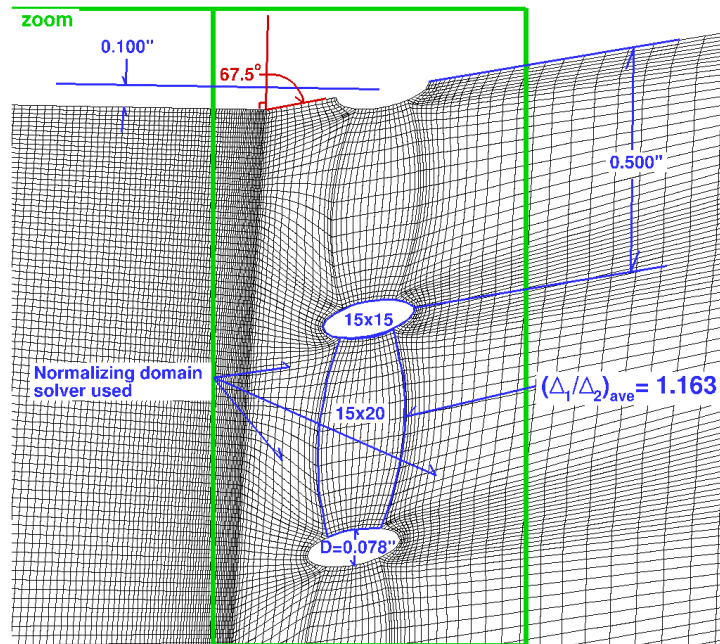
Figure 44: Cavity Bottom-Wall Grid Topology Showing Cavity Injectors (CFD++ RANS simulations) – detail
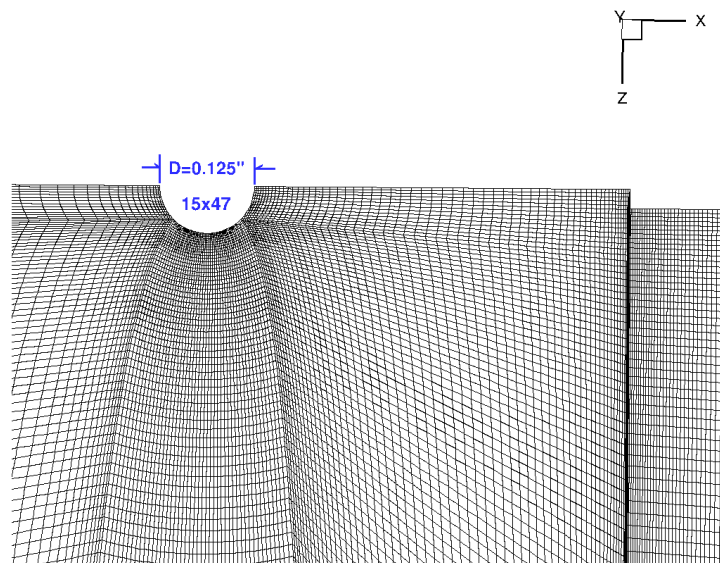
Figure 45: Cavity Bottom Wall Grid Topology of Upstream Primary Injector

Table 1: CFD++ Parameters

Input Parameter	Value	Notes
Grid	Structured	Gridgen v15
CFD++ Version	10.1.1	
Turbulence Model	RANS, cubic $k - \epsilon$	
Sc_t	0.5	
Pr_t	0.9	
Kinetics Model	TP2 (Princeton Model)	22-species ethylene combustion
Simulation type	Steady state	CFL=5.0
Inviscid Flux Limiter	Minmod	2nd order
Rieman dissipation	LHS only	less computational dissipation
Wall functions	Advective two-layer	Relaxes wall requirements, $y^+ < 50$
Heat Transfer	Adiabatic	No net heat transfer across wall boundary

simulation. The fuel injectors used the measured mass flowrate and fuel plenum total temperature as a boundary condition. The outflow was set to a supersonic outflow boundary condition. The bottom wall grid surface topology of the cavity is shown in Figure 43. Figure 44 shows the exploded view of some of the cavity injectors which have a diameter of 0.078 inches. The centerline of each injector is 0.1 inches above the bottom wall of the cavity and the ramp angle is 67.5° from the normal.

The 15×15 notation on the figure represents the number of computational nodes that span the cross-section of each cavity injector exit. There are 15×20 nodes between each injector and the average stretching ratio for the spanwise connector between each injector is 1.163, which represents the greatest average stretching in the computational domain. An elliptic smoother was used to minimize skewness. The primary injector exit is shown in Figure 45. The injector diameter is 0.125 inch with a 15×47 nodal cross-section.

All walls were modeled using a turbulent wall function with a maximum value of y^+ is 80, and were assumed to be adiabatic.

Figure 46 shows wall pressure and CFD centerline contours of static pressure and total temperature. Shown in the figure is the tare case and reacting case for the No-Shock flowpath with cavity only fueling (95 slpm). Notice there is no shock train development upstream of the cavity for the case with reactions and the pressure rise in the cavity is minimal. Contours of Mach number (not shown) were consistent in revealing that the core flow remained supersonic throughout. This means the isolator flow upstream of the cavity was largely undisturbed by the chemical reactions. Neither the experiment nor CFD saw a change in isolator wall pressure due to the addition of fuel. Two of the three isolator wall pressures compare favorably between the experiment and the CFD with the exception of the middle pressure tap (at approximately 4.5 inches). This experimental value exceeded the CFD by 13% but the other two only exceeded by 2%. The higher middle pressure was consistent throughout the test, and is likely due to a weakly reflected wave from the nozzle-isolator- interface. The cavity pressures (specifically, at approximately 11.5 inches) show a small increase in pressure between tare and reacting. The experiment showed approximately 12% increase and the CFD showed

Figure 46: Center-Line Bottom Wall Pressure and Center Plane Pressure and Total Temperature Contours for No-Shock Case with Cavity Only Fueling

approximately 20%. The two are consistent and compare reasonably well, but the CFD underpredicts the tare pressure in the cavity by approximately 10% from the experiment.

Streamwise slices of OH mass fraction in Figure 47 indicate that significant burning occurs on the cavity ramp. OH-PLIF suggests the location of burning is similar to that of the CFD. The CFD and experiment have the same general distribution of OH. Also, there is negligible spanwise variation in OH for both the CFD and experiment which suggests spanwise uniformity.

Figure 48 shows the pressure distribution for the same No-Shock case, but with both cavity and primary injector fueling. The cavity fueling rate was reduced by 50% to 47 slpm and the primary fuel injection rate was 350 slpm. The wall pressure remained mostly unchanged by the addition of primary fuel as compared to cavity only fueling shown previously in Figure 46. The CFD and experiment show a small increase in pressure towards the exit of the domain. The pressure discontinuity upstream of the cavity from the CFD data is due to the primary injection plume and is not the result of combustion.

Figure 49 shows the OH mass fraction slices for the CFD (left) and experiment (right). Along the centerline, both the CFD and experiment show minimal amounts of OH in the cavity. For this case most of the diatomic oxygen was burned, but diatomic hydrogen was present. The mass fraction of carbon monoxide was twice as much as the case with cavity only fuel. The additional fuel from the primary injector increased the fuel fraction along the centerline which burned most of the oxygen and elevated temperatures, however overall burn quality was poor. The first two off-centerline slices of OH show gradually increasing levels of OH from the experiment, the CFD did not capture this

Figure 47: CFD OH Mass Fraction Contours and Experimental OH-PLIF Imagery for
No-Shock Case with Cavity Only Fueling

Figure 48: Centerline Bottom Wall Pressure and Center Plane Pressure and Total Temperature Contours for No-Shock Case with Cavity and Primary Fueling

gradual increase and showed significantly higher levels of OH in the first off-centerline slice. The last two off-centerline slices show distinct levels of OH along the shear layer over the cavity from both the CFD and experiment.

The case with the 8° wedge in its most downstream position (Shock-On-Cavity) creates a pressure rise throughout the cavity as shown in Figure 50. With combustion the pressures in the cavity increases by 15% and the core flow remains supersonic. The CFD and experiment compare well and both show a pressure rise near the exit of the domain. It appears little burning occurs along the centerline of the cavity as shown by the low temperatures in the total temperature contour.

The first two OH slices in Figure 51 show no OH production in the CFD and minimal intensities from the experiment. The experiment shows a gradual increase in OH from one off-centerline slice to another. The CFD shows a gradual increase as well. Most of the OH occurs in the upstream portion of the cavity which is shown in both the CFD and experimental observations.

Figure 52 shows the case with the 8° wedge in its same position but with primary fuel injection. With combustion the pressure rise across the cavity is 25% greater than tare. Once again there is no thermal choking. Both the CFD and experiment show a significant pressure rise near the exit of the domain downstream of the cavity. The total temperature contour clearly shows that there is flow turning downstream of the cavity; with combustion this contributes to the downstream pressure rise.

Figure 53 shows OH slices from the CFD and experiment. A stark contrast with primary fueling can be observed on the centerline as compared to the previous case that had

Figure 49: CFD OH Mass Fraction Contours and Experimental OH-PLIF Imagery for
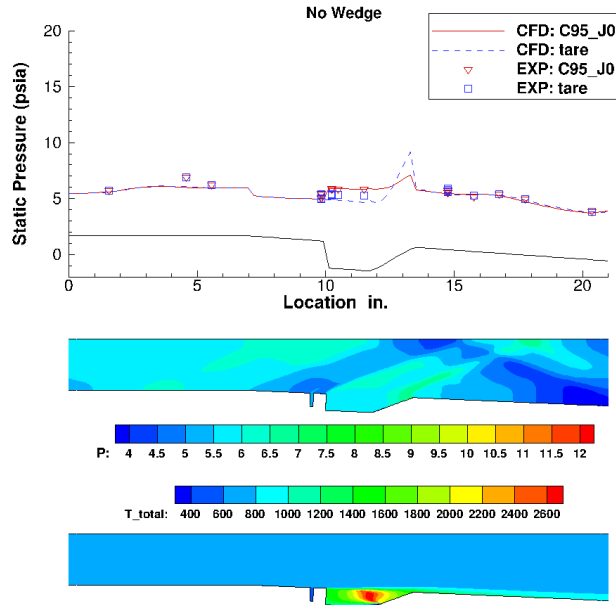No-Shock Case with Cavity and Primary Fueling
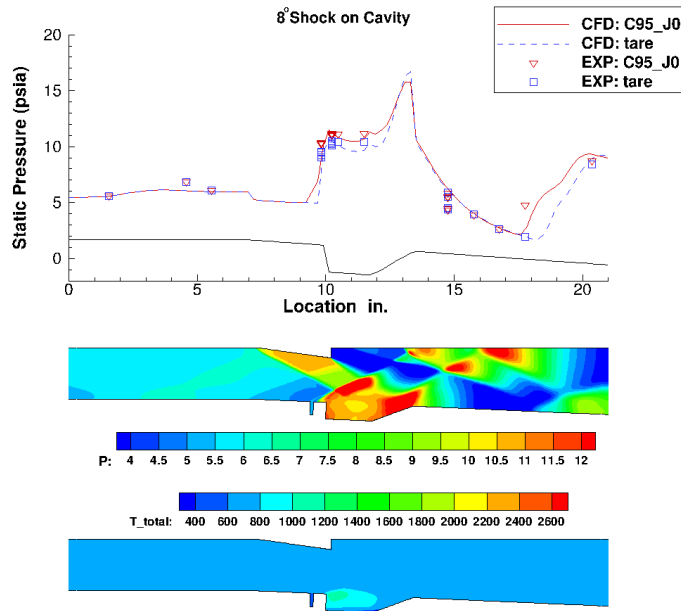
Figure 50: Centerline Bottom Wall Pressure and Center Plane Pressure and Total Temperature Contours for Shock-On-Cavity Case with Cavity Only Fueling

cavity only fuel. Both the CFD and experiment show significant levels of OH in the cavity along with elevated levels protruding into the core flow. The shape and location of OH agree very well at all spanwise locations.

The next case is the Shock-Upstream case which never lit during the experiment, thus only tare is shown in Figure 54. The pressure distribution between the experiment and CFD agree very well. Notice the strong shock that hits the upstream injector and the expansion that runs over the cavity. The next section of the analysis reviews mixing results related to this case to better understand why this case never lit.

Figure 55 shows bottom wall equivalence ratio contours for three separate mixing cases. All three cases have cavity only fueling at 95 slpm. As shown before, the No-Shock and Shock-On-Cavity cases were capable of lighting and sustaining combustion. The black cross shown in each image represents the spark plug location. The contour limits range from $0 < \Phi < 1.0$. An equivalence ratio (Φ) = 1.0 represents an ideal fuel-air mixture quantity which is the most ideal mixture for ignition from a forced ignition source. The No-Shock case shows that the spark plug is located in a region with $\Phi > 1.0$ which represents a fuel rich region. The Shock-On-Cavity case shows the spark plug exists at the edge of a fuel-rich and fuel-lean region as does the Shock-Upstream position.

Figure 56 shows a contour of Φ for the No-Shock case and the black solid line represents the axial location of the spark plug and the black dotted line represents an outline of the top of the cavity. 1D data properties were extracted along the black solid line and are shown in the 1D plot. The grey region in the 1D plot represents the flammability region for forced ignition. This region is approximate and is based on empirical flammability limits of ethylene data taken at standard atmospheric conditions. The equivalence ratio
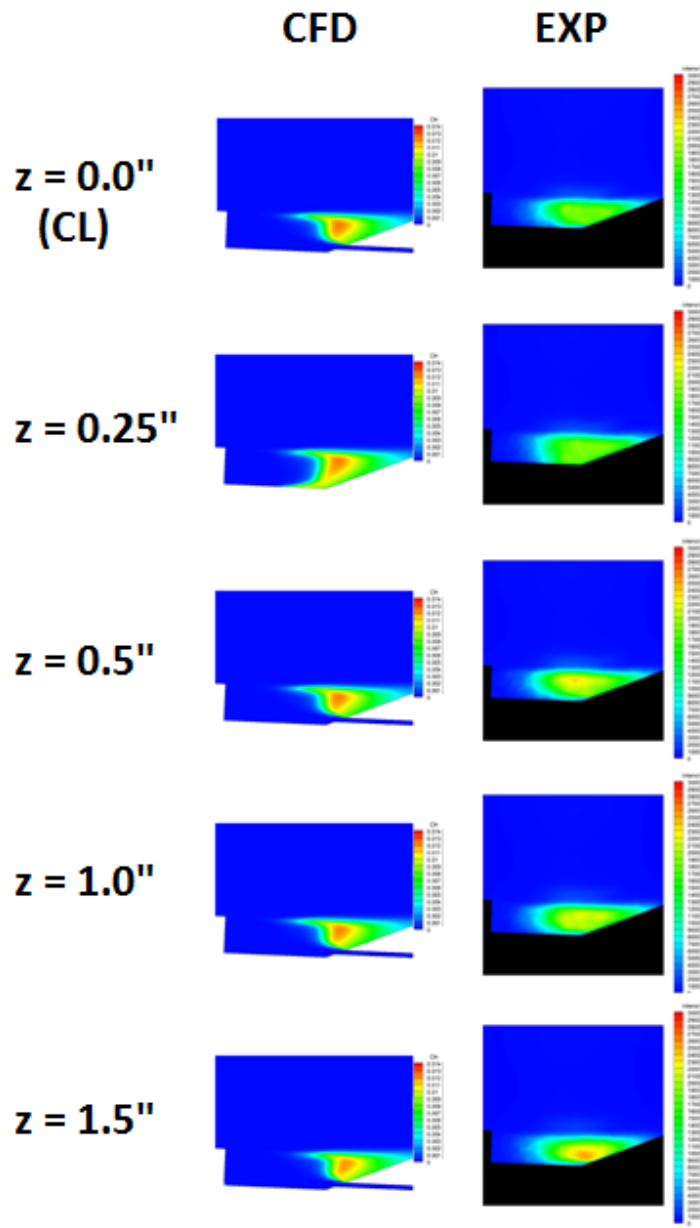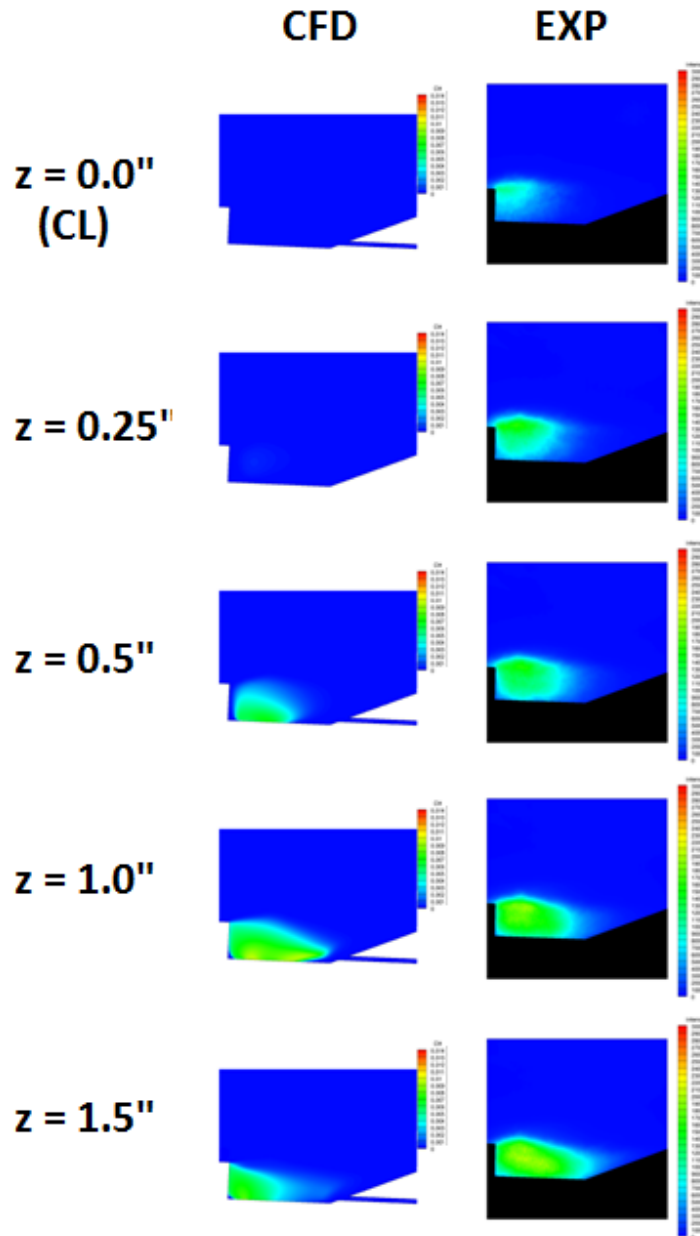
Figure 51: CFD OH Mass Fraction Contours and Experimental OH-PLIF Imagery for Shock-On-Cavity Case with Cavity Only Fueling
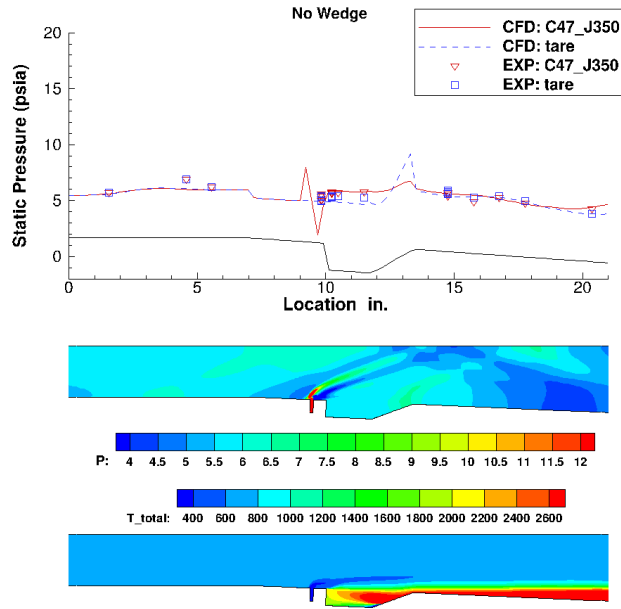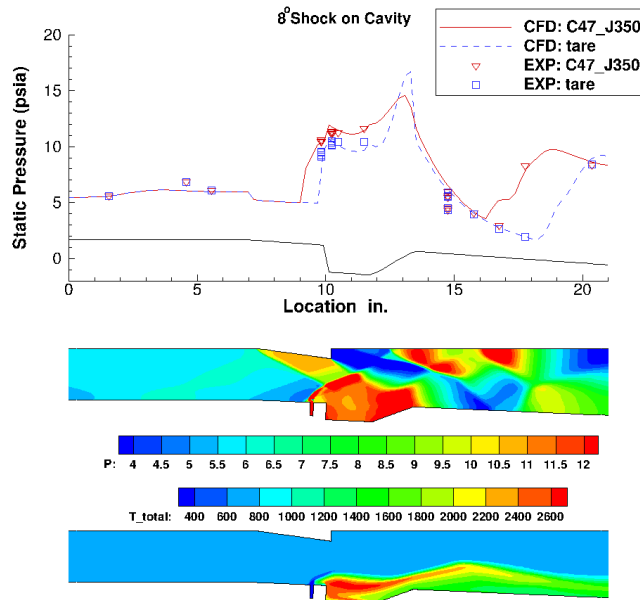
Figure 52: Centerline Bottom Wall Pressure and Center Plane Pressure and Total Temperature Contours for Shock-On-Cavity Case with Cavity and Primary Fueling

is ≈ 1.4 near the cavity floor and ≈ 1.5 along the wall normal. This means the fuel-air mixture was well within the flammability limits despite the low cavity pressure of 5 psia which is shown by the green line.

Figure 57 shows the Shock-On-Cavity case, with the wedge in its downstream position. It shows a much different Φ distribution in the cavity. The 1D shows a lean fuel-air mixture near the wall ($\Phi \approx 0.8$), but the mixture is within the lower flammability limit (LFL). Away from the wall the mixture leans out and falls outside of the flammability limits. The pressure at the wall is nearly double the No-Shock case because of the shock impinging on the cavity, the pressure is approximately 9.5 psia.

Figure 58 shows the Shock-Upstream case, with the wedge in its upstream position. This case has a very similar profile as the Shock-On-Cavity case. Near the wall and at the location of the spark plug the fuel-air mixture is lean ($\Phi \approx 0.7$), but is within the prescribed flammability limits. In contrast, the pressure near the wall is lower at 5 psia which is similar to the wall cavity pressure of the No-Shock case. Thus it appears there should have been enough fuel available to ignite the cavity given the upstream wedge position.

The following three images in Figure 59 show streamtraces coming out of the centerline cavity injector. Notice in the image on the left the fuel is entering and exiting the cavity in the same streamwise plane and the recirculation zone in the cavity is large and follows the whole perimeter of the cavity. The Shock-On-Cavity case shows a similar result as the No-Shock, except one streamtrace shows some fuel being diverted off centerline and exiting the cavity near the side wall. The Shock-Upstream position is in direct contrast to the other two. It shows the fuel entering the cavity on centerline and all the fuel exits the
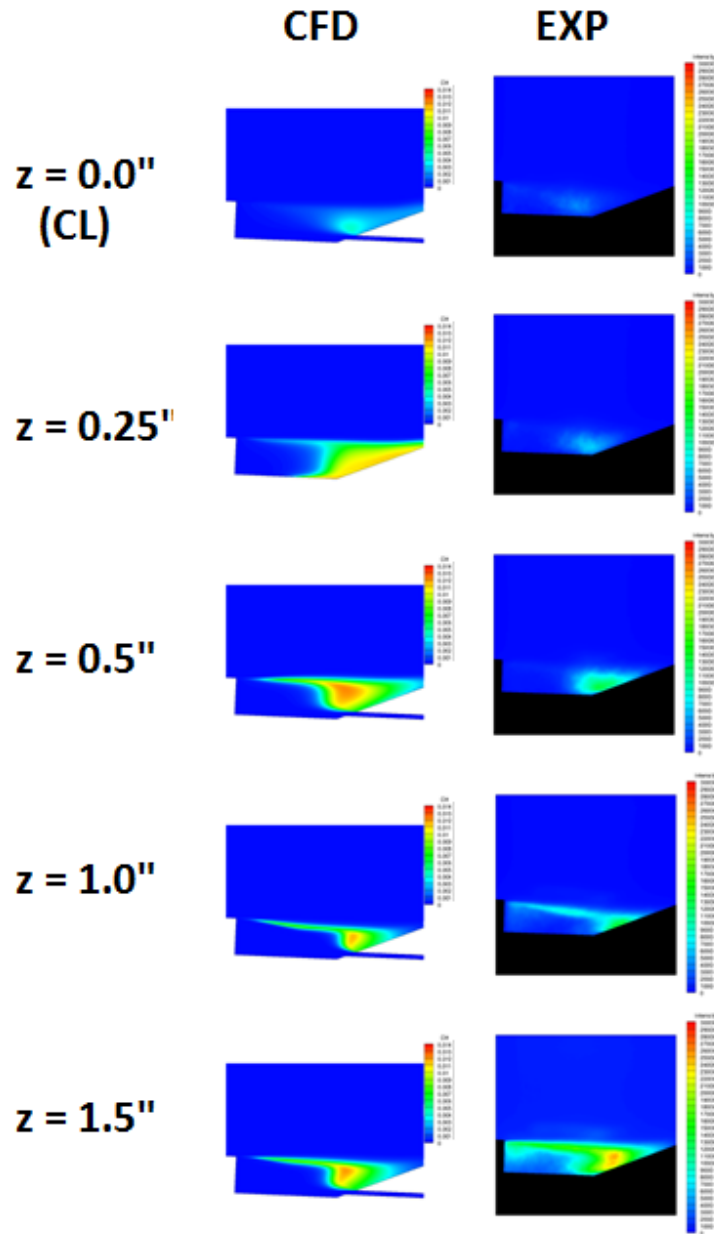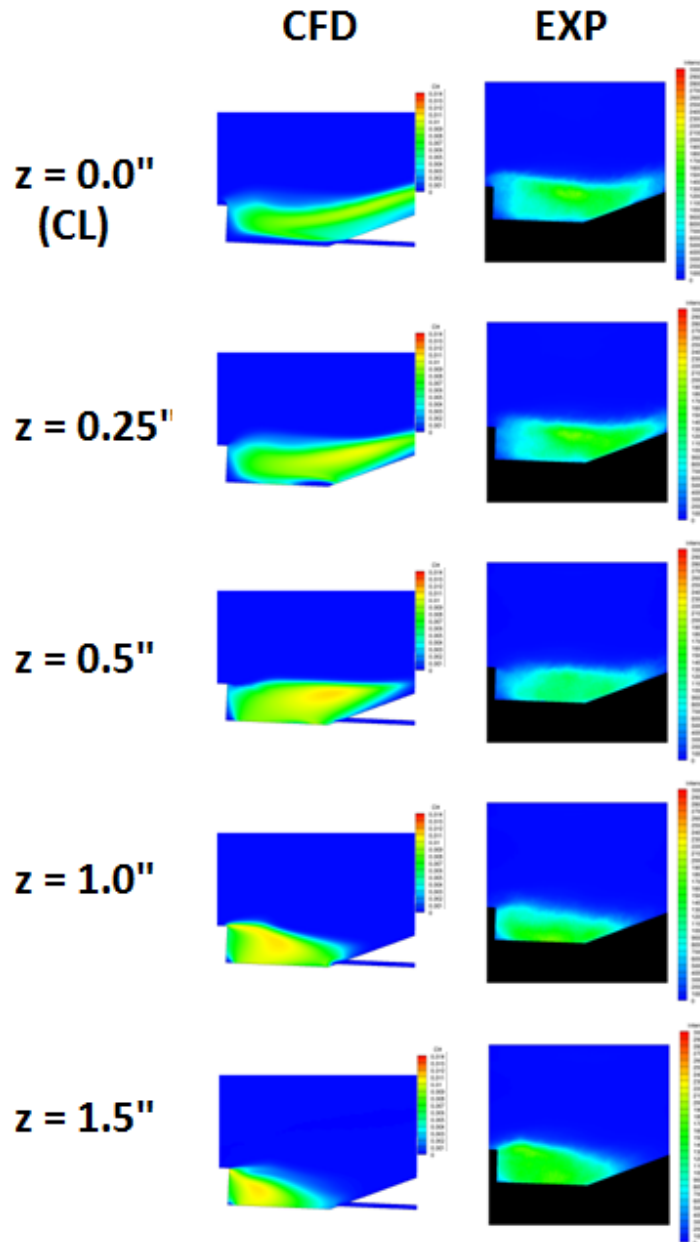
Figure 53: CFD OH Mass Fraction Contours and Experimental OH-PLIF Imagery for Shock-On-Cavity Case with Cavity and Primary Fueling
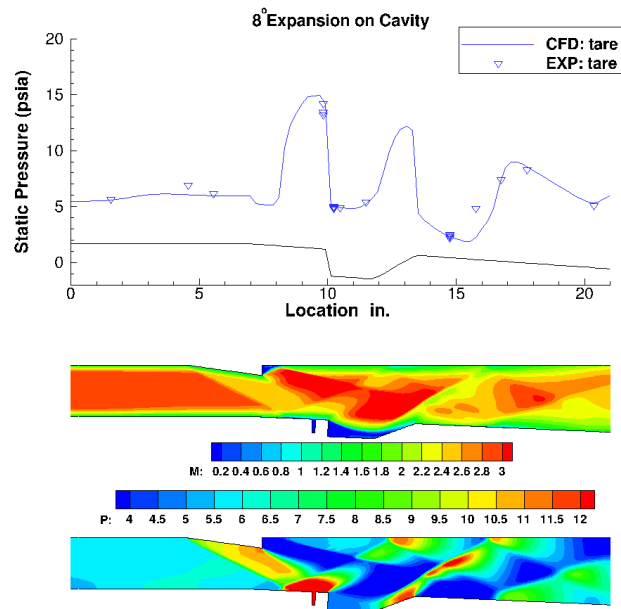
Figure 54: Centerline Bottom Wall Pressure and Center Plane Pressure and Total
Temperature Contours for Shock-Upstream with No Fueling
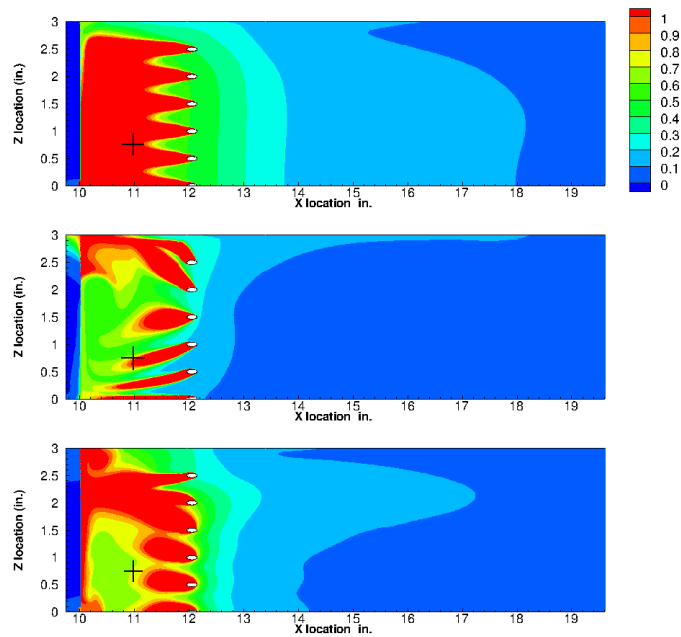
Figure 55: Equivalence Ratio Distribution on Bottom Wall for Mixing Only Cases

(from top to bottom – No-Shock case, Shock-On-Cavity case and Shock-Upstream case).
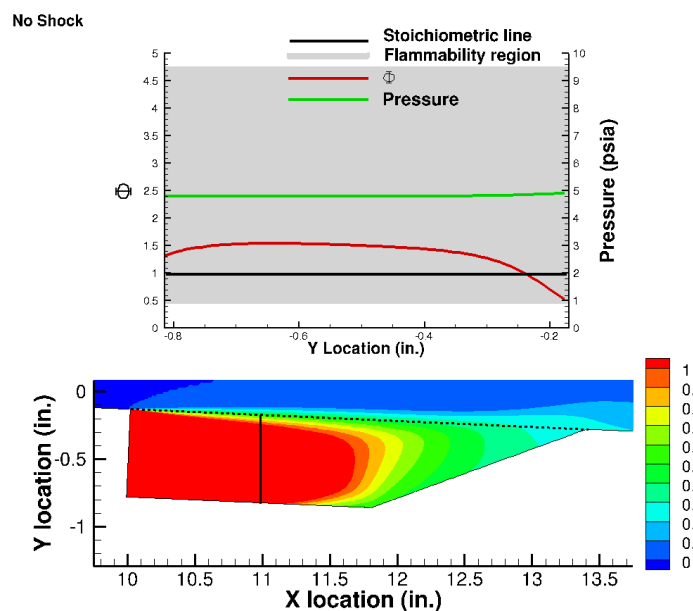
Figure 56: Center Plane Equivalence Ratio at x=11 in. Showing Flammability Limits, and Center Plane Equivalence Ratio Contours for No-Shock Case
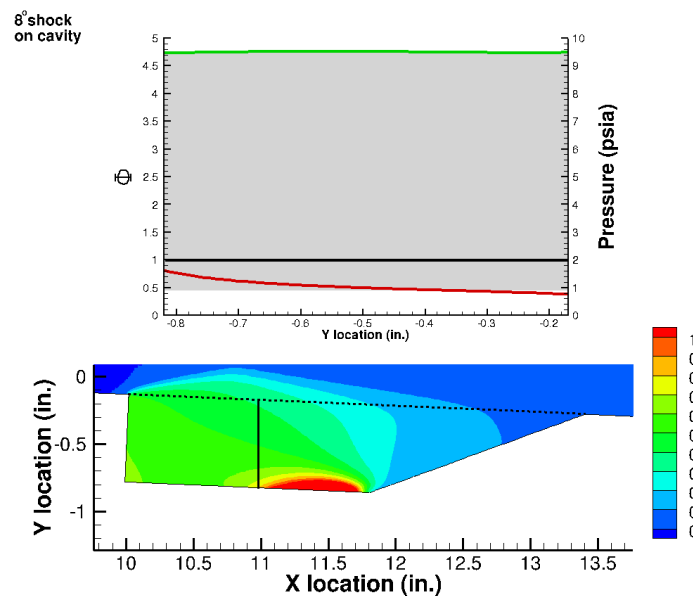
Figure 57: Center Plane Equivalence Ratio at x=11 in. Showing Flammability Limits, and Center Plane Equivalence Ratio Contours for Shock-On-Cavity Case
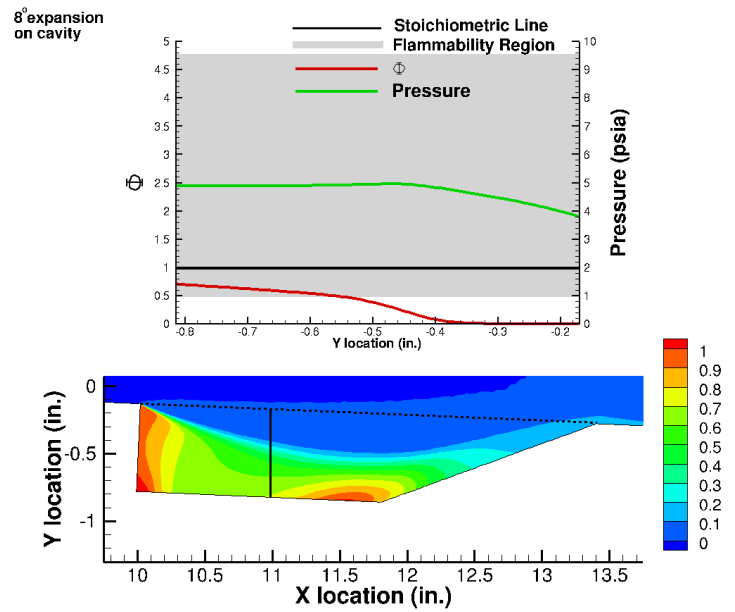
Figure 58: Center Plane Equivalence Ratio at x=11 in. Showing Flammability Limits, and Center Plane Equivalence Ratio Contours for Shock-Upstream Case

(a) No-Shock (b) Shock-On-Cavity (c) Shock-Upstream
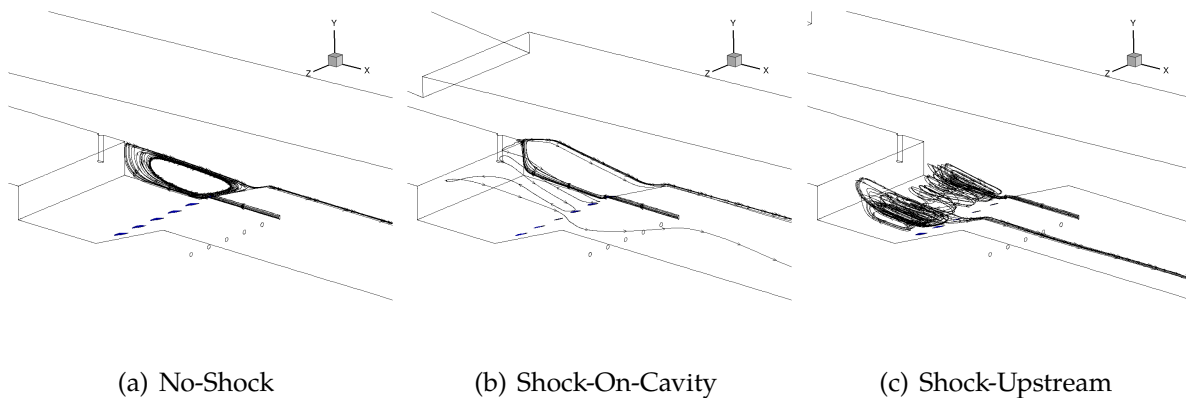
Figure 59: Cavity Fuel Streamtraces

cavity off centerline. The recirculation zone is suppressed, narrow, and does not follow the entire perimeter of the cavity.

Fine grid RANS and LES/RANS simulations

Fine grid RANS simulations of the Shock-On-Jet case with cavity only fueling were performed using the REACT-MB solver in preparation for an LES/RANS simulation of that case. For these simulations, the same grid as was used for the cold flow, Shock-On-Jet case was used. The Mawid six species, three reaction ethylene combustion model [26] was used with inert nitrogen as the seventh species. For the results shown, the Mawid model was altered so as to decrease the activation temperatures by 50%. Further investigation was not performed to assess the need for this alteration.

Figures 60–62 show a comparison between the REACT-MB results and the CFD++ results. As can be seen, there is more water present in the CFD++ contours than with REACT-MB. The hybrid LES/RANS results showed evidence of earlier burning. These results reflect instantaneous values early in the calculation, and converged mean values were not obtained during the course of this effort.

(a) CFD++ RANS (b) REACT-MB RANS (c) LES/RANS
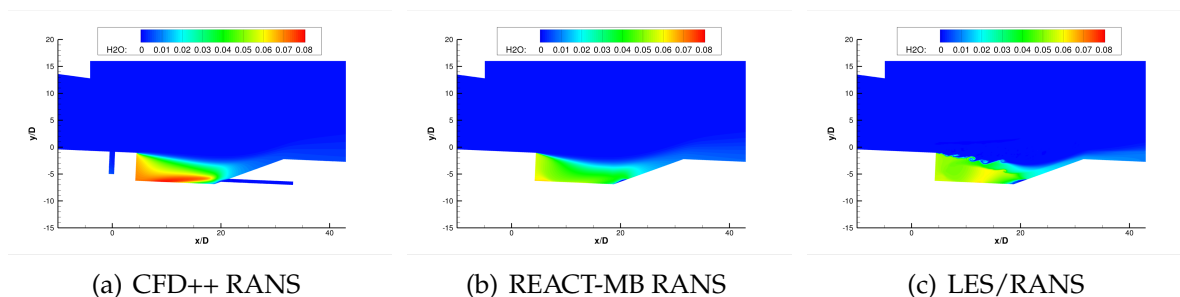
Figure 60: Contours of Water Mass Fraction at Center Plane for Shock-On-Jet Case with Cavity Fueling

(a) CFD++ RANS   (b) REACT-MB RANS   (c) LES/RANS
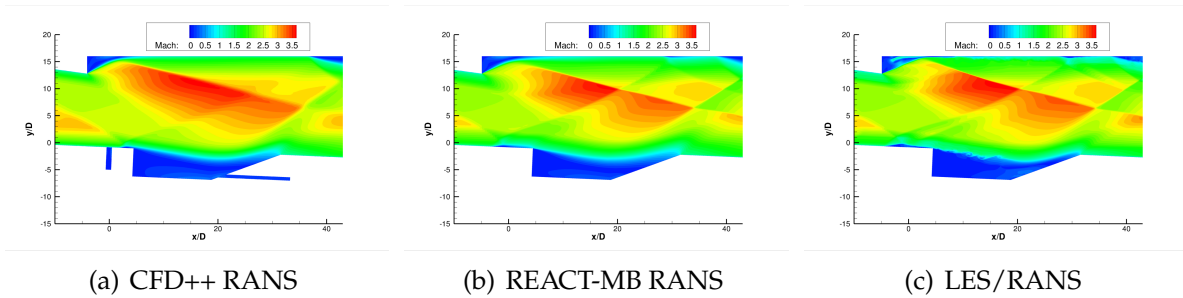
Figure 61: Contours of Mach Number at Center Plane for Shock-On-Jet Case with Cavity Fueling

(a) CFD++ RANS   (b) REACT-MB RANS   (c) LES/RANS
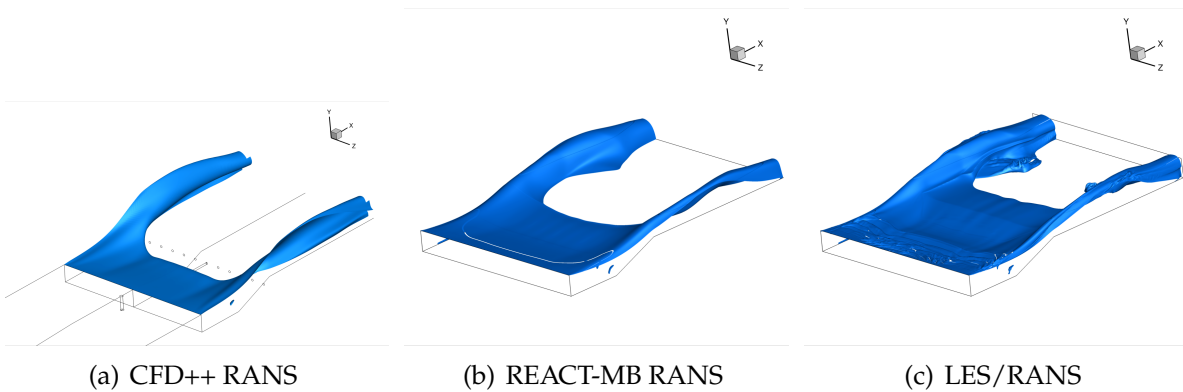
Figure 62: 3D Iso-Surface of 1% Water Mass Fraction

4.3 Nearly-Round Cross-Section Isolator

This study aimed to compare mixing characteristics for sonic injection into a supersonic crossflow, for rectangular, round, and nearly-round cross-sections. Both rectangular and round cross-sections are of technical interest, but optical access for round cross-sections is limited due to the complexity of round windows that can distort optical measurements. Hence, a nearly round-cross-section, which was derived by removing an arc of the full round cross-section, was studied to see how this geometric compromise would affect the mixing characteristics.

Studies focused on a Mach 2.0 cross-flow, with sonic injection. The RANS approach was applied for the three different flowpaths cross-sections, a 5×6 inch rectangle, a 3.9 inch diameter circle, and the same circle with a 1.875 inch wide flat surface on the bottom.

The following Figures (rectangular, circular, and semi-round from left to right) show axial slices downstream of ethylene fuel injection.

For this work a novel way of measuring fuel plume height and width was used. Instead of picking a specific injectant mass fraction (Y_f) for all the axial locations of interest and using that as the marker of the plume edge or alternately using different criteria for each location, a new method based on finding the mass fraction at which 90% of the fuel plume is contained within was used. The white lines shown in Figures 63–66 show a constant ethylene mass fraction threshold within which 90% of the mass of the fuel is contained. This allows for a single criterion to use at all locations and is used for the the plume height and width plots shown in Figures 67 and 68. In mathematical terms, one can find a mass fraction threshold (Y_t) at each axial location such that the following is satisfied:

$$0.9 \int \rho_f dA = \int \alpha \rho_f dA \tag{2}$$

$$\alpha = \begin{cases} 1, & \text{if } Y_f > Y_t. \\ 0, & \text{otherwise.} \end{cases} \tag{3}$$

Using this methodology, a consistent and meaningful criterion for determing plume edge is possible at all axial locations, which becomes valuable when analyzing plumes as they become more mixed.

Figure 68 shows that at $x/D = 0$ the fuel plume penetration for the semi-round configuration closely approximates that for the fully round case. In addition, Figure 67 shows that the lateral plume spreading for the semi-round is also quite close to the round case. This behavior confirms the assumption that a semi-round configuration would provide similar global mixing as a fully round configuration, and therefore the semi-round case, with its potential for allowing optical diagnostics through the flat wall, should be considered for fundamental diagnostic evaluation of fuel injection in round combustors.

Figure 63: Contours of fuel mass fraction at x/D = 0

white line indicates 90% ethylene mass threshold, Y_t.

Figure 64: Contours of fuel mass fraction at x/D = 5

white line indicates 90% ethylene mass threshold, Y_t.

Figure 65: Contours of fuel mass fraction at x/D = 15

white line indicates 90% ethylene mass threshold, Y_t.
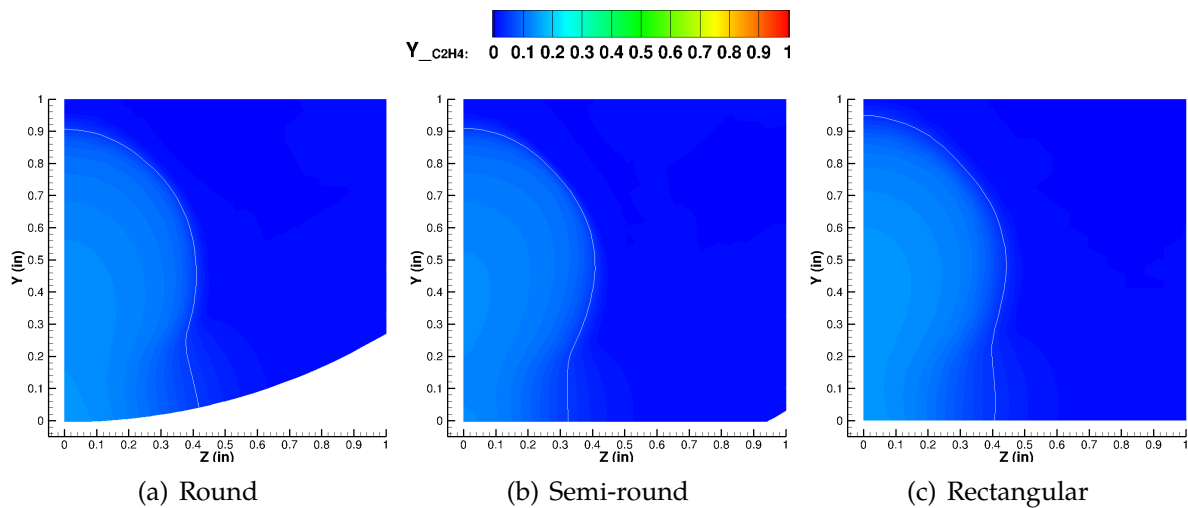
Figure 66: Contours of fuel mass fraction at x/D = 25

white line indicates 90% ethylene mass threshold, Y_t.
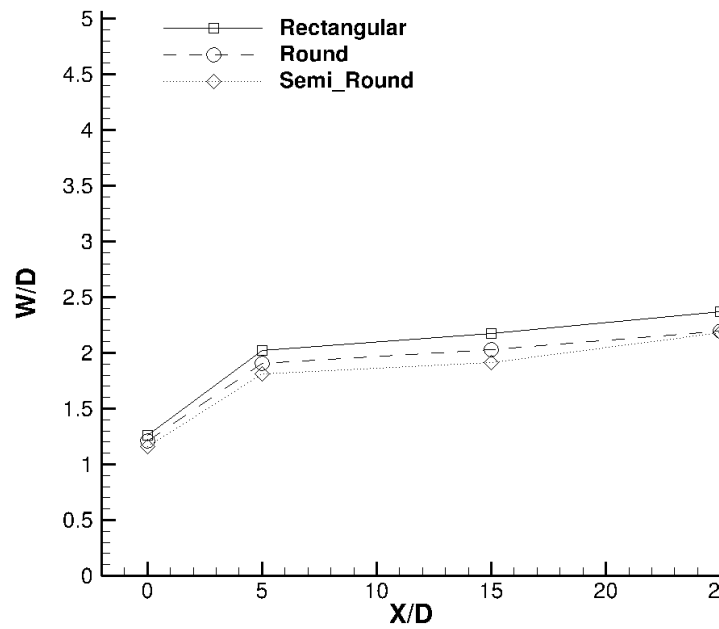
Figure 67: Plume Width Comparisons
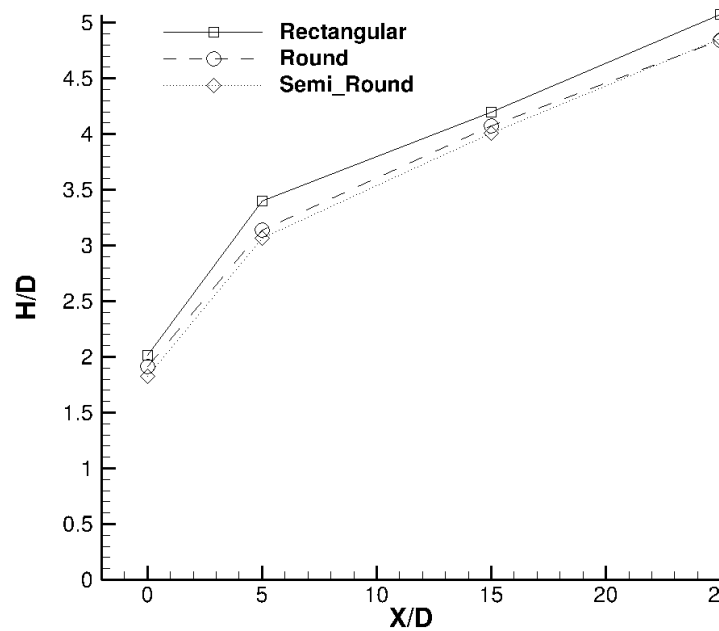
Figure 68: Plume Height Comparisons

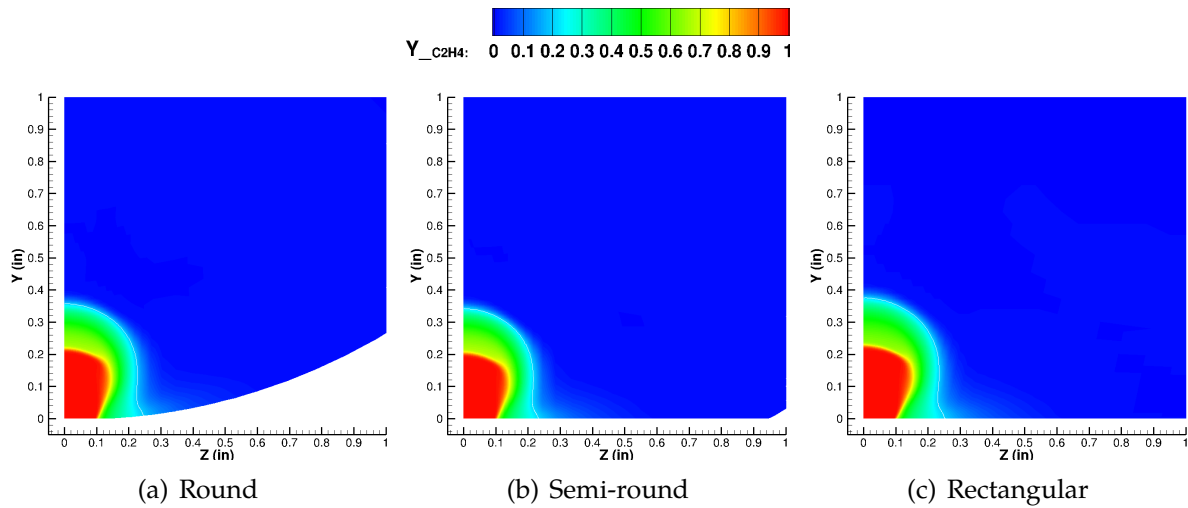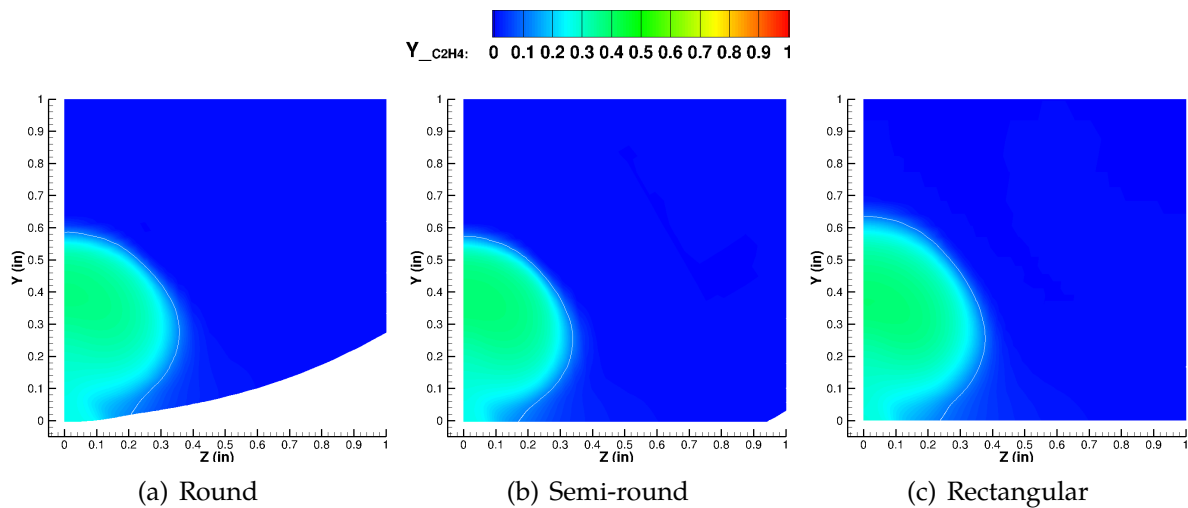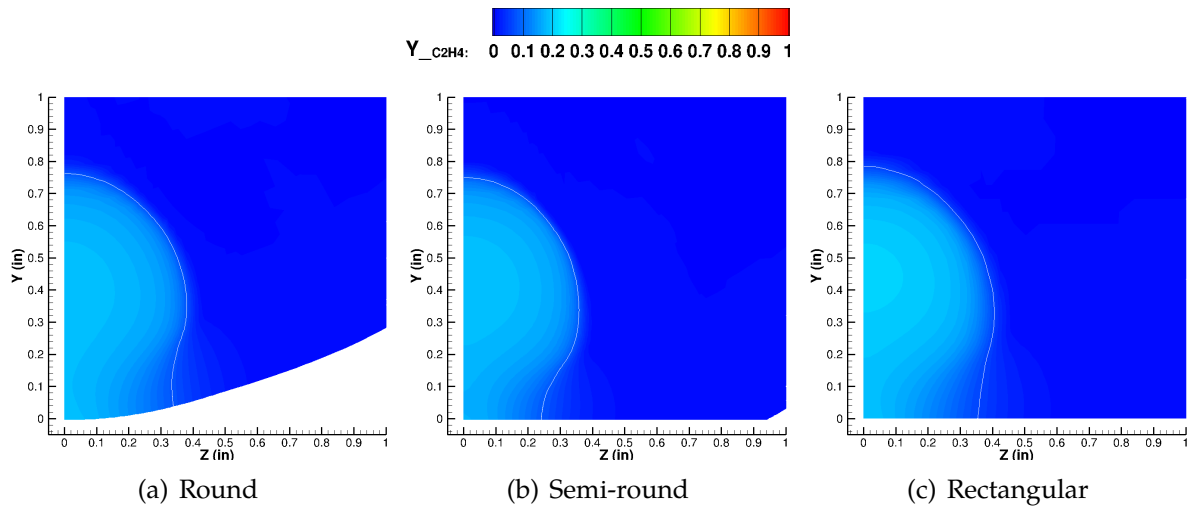Table 2: One-Dimensionalized CFD Conditions Two Duct Heights Downstream of Isolator Entrance for Inlet Configuration

Condition	Value
Mach Number	2.693
Mass Flow (kg/s)	25.20
Pressure (kPa)	101.4
Total Pressure (kPa)	2380.0
Total Temperature (K)	1792

4.4   Round Cross-Section Distortion

Analysis of distortion generation has actively been pursued. The purpose of distorting isolator flow to the combustor section of a scramjet engine is to mimic the distortion that would propagate into an isolator from an inlet of a flight vehicle. Many facilities are not large enough to perform free-jet testing of scramjet engines which include an inlet. Rather, testing is often limited to direct connect facilities. These facilities provide flow conditions that are consistent with the average conditions expected in flight, but do not reproduce the aerodynamically complex flow features that are inherent to inlet compression producing distortion. Two design concepts for the direct-connect setup have been explored for replicating the distortion from the inlet study. The first is an air injection device, which injects air to produce the desired shocks and flow features from the inlet study. The second design concept is the implementation of an intrusive device that can replicate the distortion effects. The present work focuses on the intrusive device concept.

The target conditions for the distortion generator are derived from the flow quantities entering the isolator from CFD analysis of a representative inlet and isolator. In the present analysis, these conditions are for flight at Mach 6 and 4 degrees angle of attack, and the isolator has a diameter of 12 inches. Figure 69 shows computational data from the inlet analysis. The solution extracted at the slice extraction plane is used to define the target average conditions and the targe profiles of the flow variables.

The direct-connect distortion generation devices are assessed by comparing the average distortion generator exit flow quantities to the inlet exit and then comparing the overall flow features and structures.

The in-stream location that was chosen from the inlet data was located 2 duct heights downstream (24 inches) of the isolator entrance which is referenced axially at $x = 0$. Significant compression takes place on the cowl of the inlet and those shocks propagate through the isolator. The flow turning and the longer length on the body side causes a significant thickening of the boundary layer which can be observed on the upper surface which spans approximately 30 degrees circumferentially; the Mach contour in Figure 69 shows this. The contour on the lower right shows axial mass flux (ρU) which shows that much of the mass is concentrated in the core. Features like these are to be replicated using the distortion generating device. The average quantities at this location in the isolator for the inlet study are shown in Table 2.
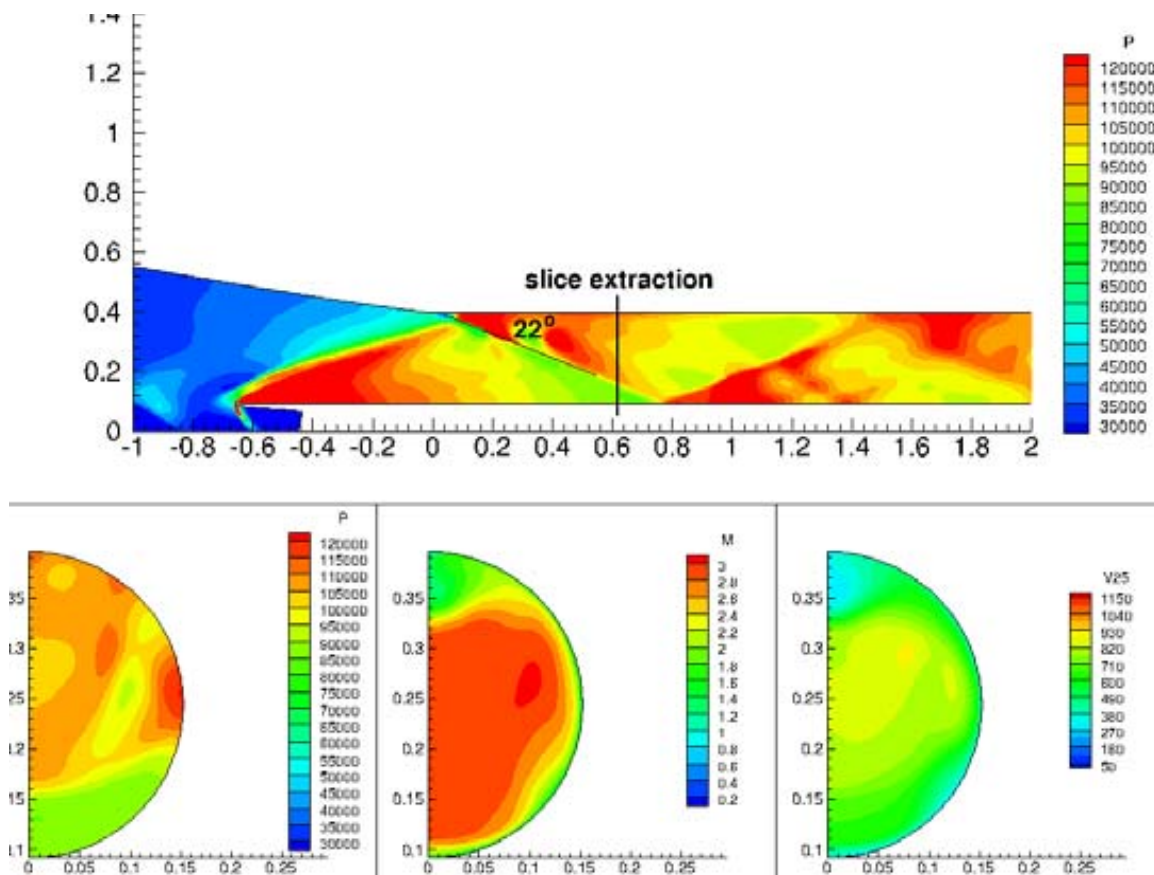
Figure 69: Flight Simulation Results
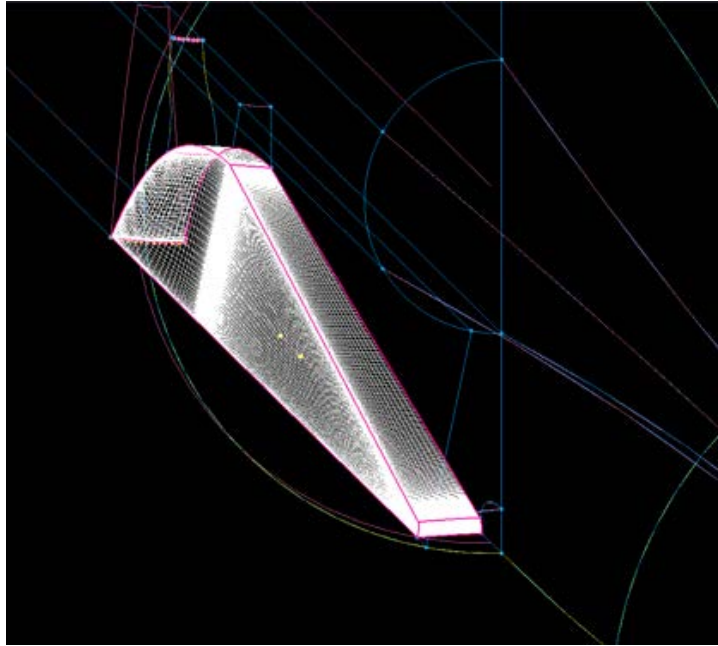
Figure 70: Iteration 3 Design Grid Section

Listed are five intended goals of the direct-connect distortion generation device. An assessment ranking the ability for each design to meet these goals is made in this analysis:

I. To replicate the averaged flow quantities from the inlet configuration's isolator flow.

II. To replicate the structures and distorted flow features from the inlet configuration's isolator flow.

III. To achieve the desired flow quantities and features in the shortest isolator length possible.

IV. For a single distortion generation device to be viable to simulate flight-like distortion at varying flight conditions and AOAs.

V. Ease of manufacturability of the intrusive device.

Eight intrusive devices were explored in this analysis. Each device was progressively and generically named starting with iteration 1 (it1) through iteration 8 (it8). Five of the devices provided unique insight, and the motivation for progression from one device to the next is described in the following paragraphs.

Iteration 3

The first two distortion devices, it1 and it2 were minimally intrusive designs that did not block nearly enough of the flow to replicate the inlet distortion, thus they are not
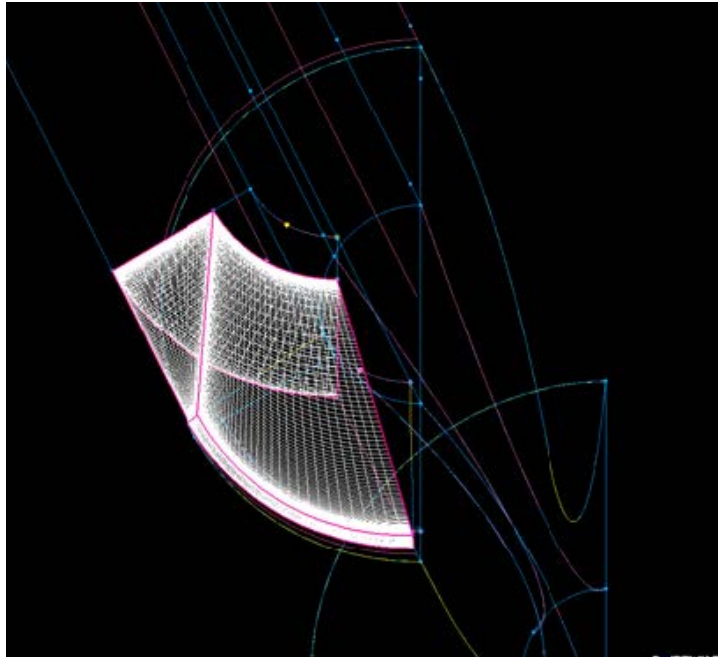
Figure 71: Iteration 4 Design Grid Section

explored further in the results section. The third concept, also conservative, is shown in Figure 70. This device, unlike the previous two, did provide useful information for future designs.

This wedge had a 22 inch long compression surface that penetrated deeply into the flow achieving maximum height of 2.75 inches. It had a 7 inches rounded trailing edge to relieve the strength of the expansion. The wedge was narrow and only spanned 10 degrees circumferentially for a half geometry setup. The maximum physical area blockage as a percentage of the unblocked isolator area was 4.8%. This was not nearly enough blockage needed to achieve the averaged 1D flight like quantities, but features such as a long compression surface and relieved trailing edges are part of other designs that were explored. The summary of all 1D quantities is shown in the summary section.

Iteration 4

This device is a derivative of it3, it too had a 22 inch compression surface that had a maximum penetration of 2.75 inches. Unlike it3 it did not incorporate any kind of trailing edge expansion relief and it spanned 60 degrees circumferentially. The greater circumferential span increased the maximum area blockage to 23.3%. Figure 71 shows the outline of the device. Figure 72 shows contours of the flowfield including the best selected x-slice to be compared to the flight.

This concept finally appeared to be in the range of shock strength needed to simulate the shock strength from the inlet, although this design slightly overshocks the flow. The boundary layer profile is similar to flight but appears separated from the wall surface.
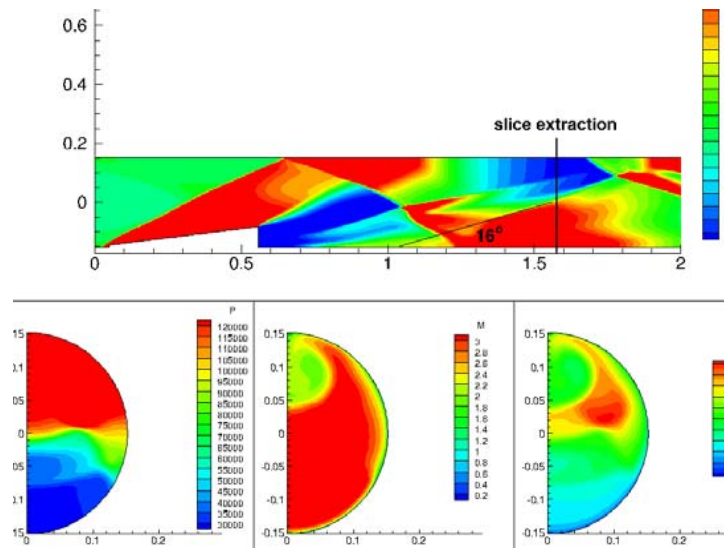
Figure 72: Iteration 4 Contours of Pressure, Mach Number and Axial Mass Flux (ρu).

The expansion off the trailing edge significantly disrupts the desired flowfield features.

Iteration 6

This device was again a 60° circumferential device, but it implemented a fully contoured body. Along the centerline at 0° circumferential a maximum penetration of 2.25 inches which was a half inch less than its previous counterparts. At the 60° circumferential station, the penetration was only 1.25 inches making it a non-uniformly penetrating device. The maximum blockage was 16.6%. The reason for non-uniformity in the contour was meant to mimic the low pressure pocket which was observed in the inlet data. Figure 73 shows the device. Figure 74 shows contours of the flowfield including the best selected x-slice to be compared to the flight.

This concept again produced desired shock strengths, but the contoured trailing edge did not relieve the expansion as much as was anticipated. The boundary layer profile is attached, but again the expansion off of the trailing edge distrupts too much of the flowfield. It was becoming apparent that in order to achieve enough blockage the device would have to penetrate deeply and be excessively long to relieve the effects of the expansion. Another idea was to not make the device any longer but to reduce the penetration which would help minimize some of the effects of the expansion, but in order to achieve the necessary area blockage the device would need to span beyond 60 degrees circumferentially.

Iteration 7

This device spanned 120° circumferentially and at the 0° circumferential station its maximum penetration was 1.5 inches and at the 120° it was only 0.75 inches. This device

Figure 73: Iteration 6 Design Grid Section
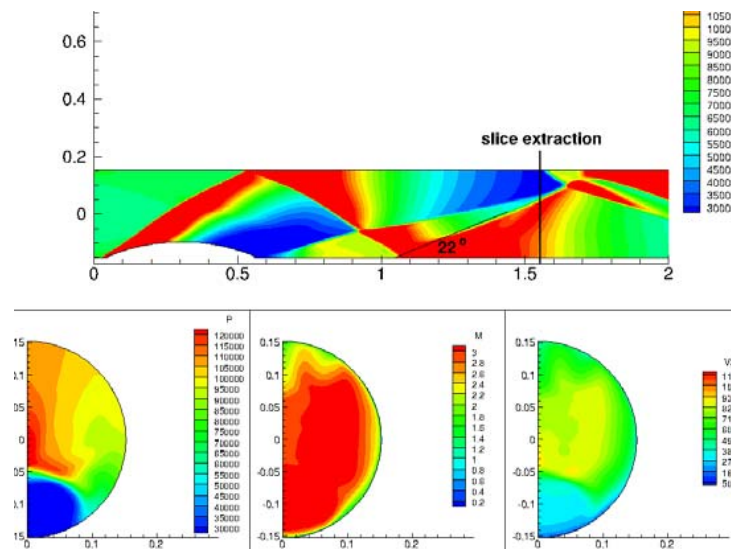
Figure 74: Iteration 6 Contours of Pressure, Mach Number and Axial Mass Flux (ρu).

Figure 75: Iteration 7 Design Grid Section

Figure 76: Iteration 7 Contours of Pressure, Mach Number and Axial Mass Flux (ρu)

<table>
<tr><td>(a) Flight-like simulation</td><td>(b) Design iteration 7</td></tr>
</table>

Figure 77: Pressure Isosurface (P = 100kPa) for Flight-Like Simulation and Design Iteration 7

was also nonuniformly configured with a relief for the expansion. The maximum physical area blockage for this device was 21.4%. Figure 75 shows this device. Figure 76 shows contours of the flowfield including the best selected axial position to be compared to the flight.

This concept appears to have a fully attached boundary layer profile although the thickness is significantly reduced. The strength of the expansion is also reduced, but the downstream shock strengths are weak as compared to the flight. It does appear that greater circumferential span is needed to achieve flight like features.

One fundamental flaw with the intrusive devices up until this point was observed. It appears that shocking down the flow all at the same axial location creates non-flight like features. Figure 76 shows this.

The iso-surface contours in Figure 77 show pressure at 100 kPa for the flight-like inlet and design iteration 7. The pressure wave from the crotch of the inlet forms an elliptical shape as it propagates into the isolator. Iteration 7, initiates a conical shock at one axial location but the pressure wave appears to swirl as it propogates which is not a feature observed from the inlet data. All of the distortion device concepts up until this point suffered from this phenomena at varying degrees of severity. This was all considered for the next concept.

Iteration 8

The iteration 8 design has been given the name "boomerang wedge." It is a 180°, nonuniform, axially swept distortion generation device with relief. Unique features of this device include distributed shocking of the flow rather than all at one axial location
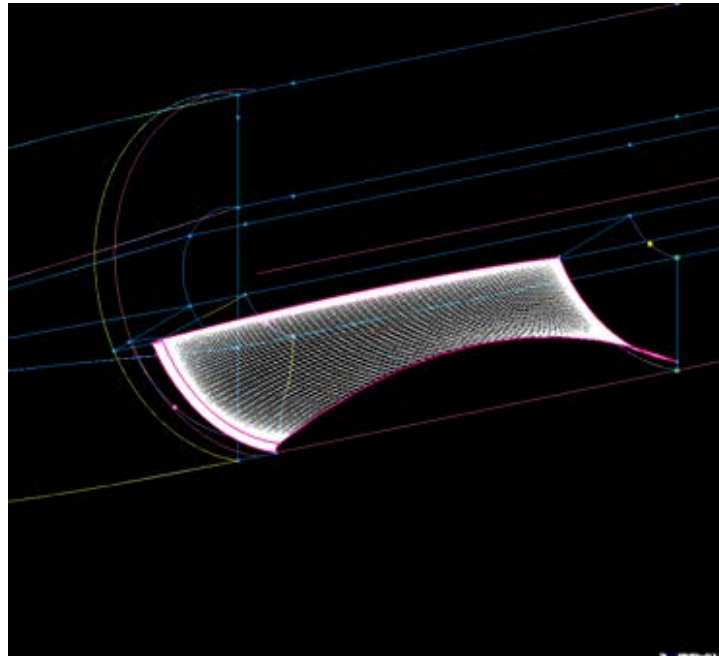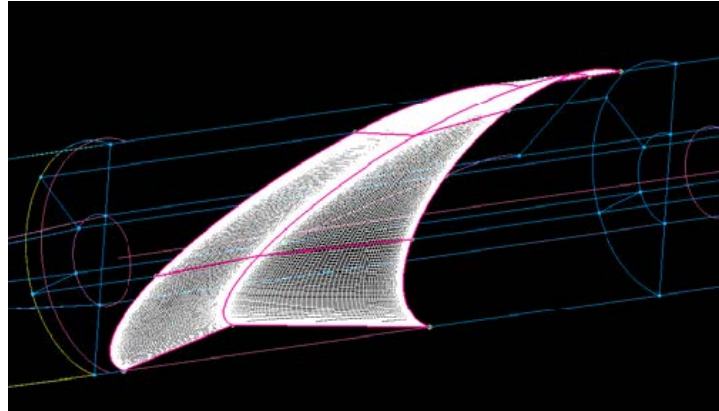
Figure 78: Iteration 8 Design Grid Section
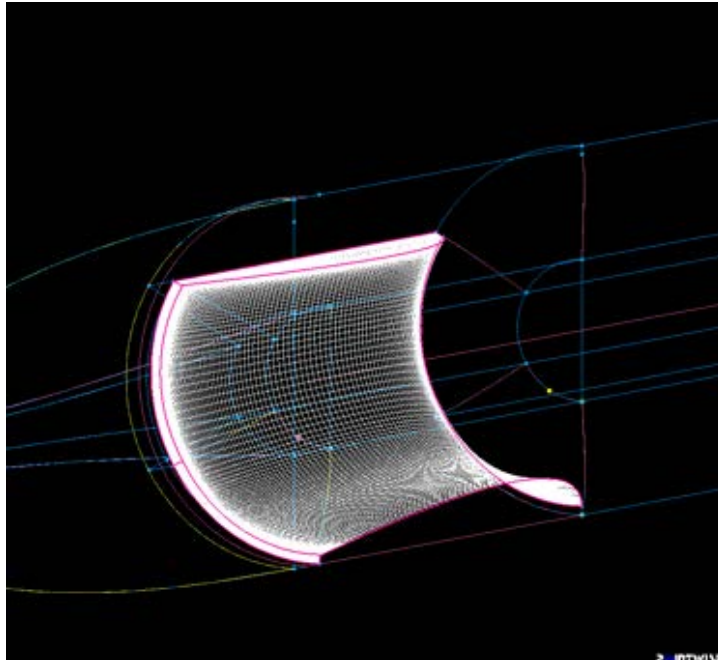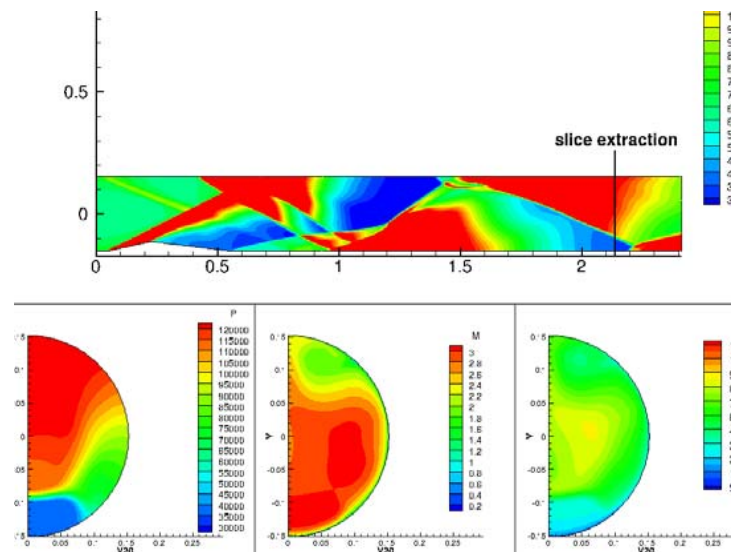

Figure 79: Iteration 8 Contours of Pressure, Mach Number and Axial Mass Flux (ρu)

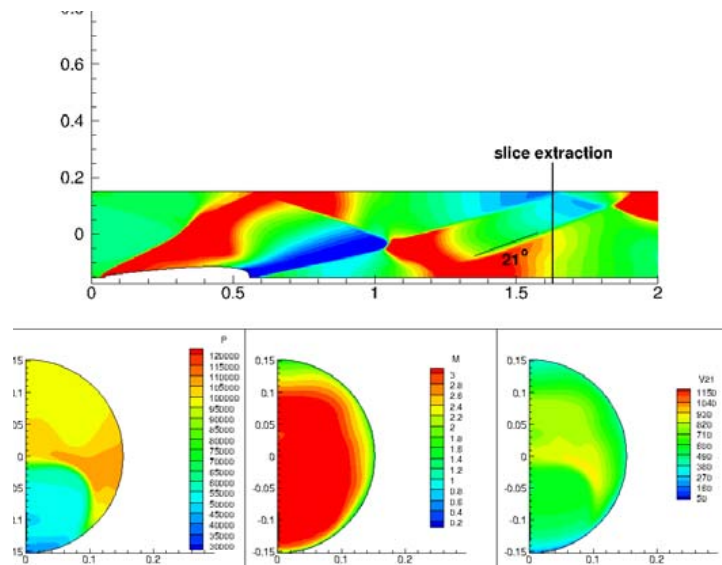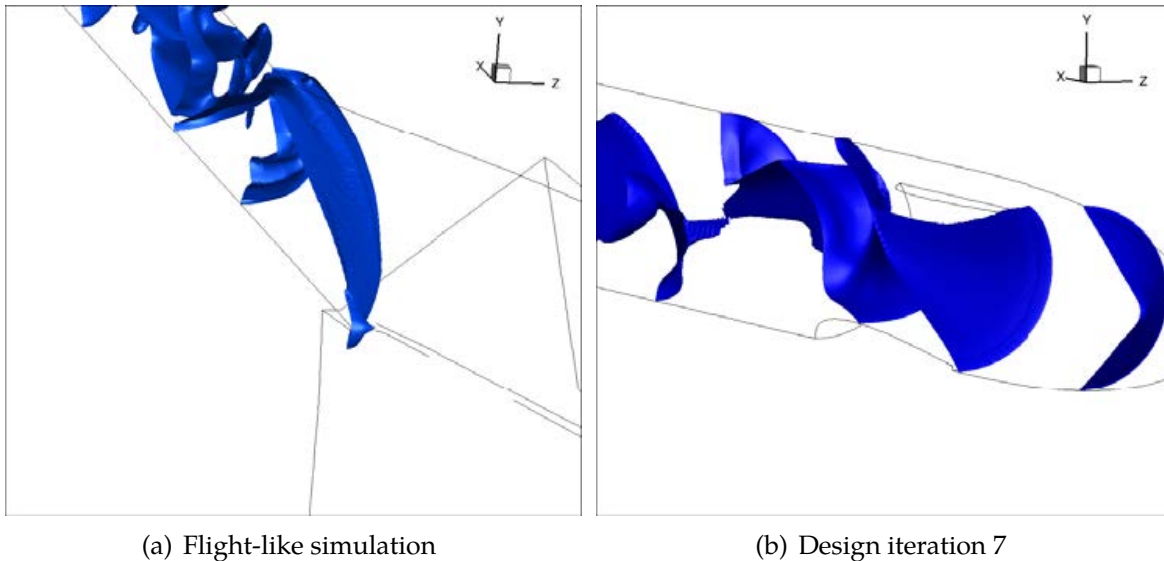(a) Flight-like simulation   (b) Design iteration 8
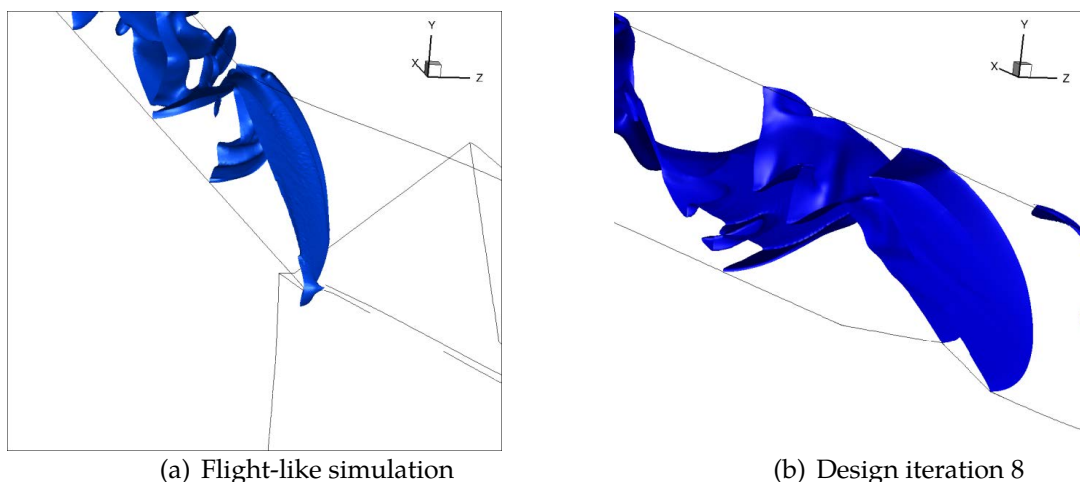
Figure 80: Pressure Isosurface (P = 100kPa) for Flight-Like Simulation and Design
Iteration 8

like the previous designs. This device is not contoured like some of the other devices and
at the $0°$ circumferential station it has a maximum penetration of 1.5 inches and is axially
and circumferentially swept $180°$ to 0 inch penetration. The overall length of the
intrusive device is approximately 30 inches. Since the device gradually blocks the flow
the assessment of maximum area blockage is not entirely accurate but this device has a
physical area blockage of approximately 15.2%. Figure 78 shows this device. Figure 79
shows contours of the flowfield including the best selected x-slice to be compared to the
flight.

This device produces features very similar to the flight. The boundary layer profile
appears attached but is slight offset circumferentially. The flow still suffers from strong
expansions off of the trailing edge of the distortion device. However this device better
replicates the elliptical shock pattern that was observed propogating from the crotch of
the inlet, which is shown in Figure 80.

The angle of sweep for the distortion generating device was not enough as the flow
collapses in to the flowfield at the core which is what causes the double shock effect
which is observed in the previous contour. Adjustment to this design, including sweep
angle or leading edge angle can be made to achieve a more flight like elliptical shock
pattern.

Iteration Summary

Table 3 summarizes the 1D averaged properties at the selected axial slice for each of the
iterations observed in this analysis.

It8 performed the best in terms of average Mach number, static pressure, and total
pressure, but it8 has some serious flaws which are outlined in Table 4 which provides an
assessment ranking for each design, using the goals that were established above. The

Table 3: One-Dimensionalized CFD Conditions Two Duct Heights Downstream of Isolator Entrance for Inlet Configuration

Condition	Flight-like	It3	It4	It6	It7	It8
Slice position (duct heights)	2	5	5	5	5	7
Mach number	2.69	3.20	2.92	2.93	3.01	2.69
Mass flow (kg/s)	25.2	23.23	23.23	23.23	23.23	23.23
Pressure (kPa)	101.4	76.2	89.0	91.3	84.8	100.1
Total Pressure (kPa)	2380	4632	3428	3557	3768	2611
Total Temperature (K)	1792	1704	1693	1697	1702	1676

Table 4: Assessment of Each Design Toward Meeting Goals

Goal	It3	It4	It6	It7	It8
I	1	3	3	2	5
II	1	2	3	2	4
III	3	3	3	3	1
IV	N/A	N/A	N/A	N/A	N/A
V	5	5	3	3	1

rating scale is subjective, with (1-very unfavorable, 2-unfavorable, 3-moderate, 4-favorable, and 5-very favorable).

5   Conclusions

RANS and hybrid LES/RANS computation models have been applied to various problems related to flow distortion in scramjet flows. For the cases where supporting experimental data is available, good agreement has been shown. In addition to the insights gained on the validity of the computational models, we have gained insight into the effects of flow distortion.

Hybrid LES/RANS simulations of sonic injection of ethylene into a Mach 2 crossflow have been compared with new experimental NO-PLIF and high-frequency shadowgraph imagery of air injection with inflow distortion. The impact of the tested 5-degree shock generator on mixing has been shown was shown to be minimal. The LES/RANS model was very capable of predicting the mixing and the impact of the 5-degree shock generator on the mixing of the injectant. A 7-degree shock generator configuration was also simulated, though that has not been tested experimentally yet. This configuration shows even more mixing than the 5-degree generator due to further slowing of the flow. Unfortunately this shock causes a large separation in the wall boundary layer as well as a significant drop in total pressure.

RANS and hybrid LES/RANS were used to simulate shock distortion for cavity-assisted mixing and combustion. The shock impingement in the cavity region was shown to have a significant effect on both the non-reacting flow, in which the shear layer over the cavity was either lifted or depressed dependent on the shock position relative to the cavity. Both RANS and LES/RANS models accurately modeled this displacement of the shear layer. This effect carried over into the reacting studies, where the ability to ignite the cavity was fundamentally changed by the location of the shock. RANS simulations showed some good agreement with the cases that did ignite experimentally, but no attempt was made to model the case where no ignition occurred. However, a non-reacting simulation of the non-igniting case shed light on possible causes of the ignition issue.The combusting hybrid LES/RANS simulations were not completed, but showed potential for high-quality predictions. Further pursuit of hybrid LES/RANS simulation of combusting ethylene is recommended.

RANS studies of the nearly-round cross-section isolator flowfield showed that the gross penetration and mixing characteristics were similar to the fully-round cross-section, indicating that the nearly-round approach would be a valid approach to studying mixing for round cross-sections. The value of the nearly round cross-section approach lies in the ability to support planar laser diagnostics such as PLIF. Further investigations of this approach, including hybrid LES/RANS simulations is recommended.

Finally, a series of design iterations were studied using RANS, aimed at developing an intrusive device that would provide flow distortion similar to a flight inlet. The main challenge to mimicking flight like distortion using an intrusive device was balancing the area blockage needed to obtain the 1D flow properties and minimizing the strengths of the expansions on the trailing edge of the devices. Strong expansions created non-flight like features in the flowfield. Long lengths and multiple shock reflections were needed to reduce the effect of the expansions. Expansions could be partially mitigated by

increasing the circumferential span of the intrusive device. Axial sweeping of the device also produced better flight like features.

Further analysis can explore using wedge sweeping designs that are easier to manufacture. Also, a combination of an intrusive device that utilizes air injection on its relief ramp could help reduce the strength of the expansion. At the same time this could minimize the amount of air needed by an injection-only design to produce the desired distortion effects because the intrusive device would be providing the majority of the blockage. This could also help reduce distortion duct length. This combination would make an intrusive device more flexible at varying flight conditions and could mitigate the need for multiple intrusive devices to match each flight condition.

6 References

[1] Schetz, J. A., Maddalena, L., and Burger, S. K., "Molecular Weight and Shock-Wave Effects on Transverse Injection in Supersonic Flow," *Journal of Propulsion and Power*, Vol. 26, No. 5, September 2010, pp. 1102–1113.

[2] Campioli, T. L., Maddalena, L., and Schetz, J. A., "Studies of Shock Wave/Transverse Injection Interaction on Supersonic Mixing Processes," AIAA Paper 2006–8135, Canberra, Australia, July 2010.

[3] "NASA Hyper-X Program Demonstrates Scramjet Technologies," FS-2006-01-118-LaRC.

[4] Palekar, A., Truman, C. R., and Vorobieff, P., "Prediction of Transverse Injection of a Sonic Jet in Supersonic Crossflow," AIAA paper 2005-5366, Toronto, Ontario, June 2005.

[5] Boles, J. A., Edwards, J. R., and Baurle, R. A., "Large-Eddy/Reynolds-Averaged Navier-Stokes Simulations of Sonic Injection into Mach 2 Crossflow," *AIAA Journal*, Vol. 48, No. 7, July 2010, pp. 1444–1456.

[6] Maddalena, L., Campioli, T. L., and Schetz, J. A., "Experimental and Computational Investigation of Light-Gas Injectors in Mach 4.0 Crossflow," *Journal of Propulsion and Power*, Vol. 22, No. 5, 2006, pp. 1027–1038.

[7] Spalart, P. R., Jou, W.-H., Strelets, M., and Allmaras, S. R., "Comments on the Feasibility of LES for Wings and of a Hybrid RANS/LES Approach," *Advances in DNS/LES*, edited by C. Liu and Z. Liu, Greyden Press, Dayton, OH, 1998, pp. 137–147.

[8] Spalart, P. R., Deck, S., Shur, M. L., Squires, K. D., Strelets, M., and Travin, A., "A New Version of Detached-Eddy Simulation, Resistant to Ambiguous Grid Densities," *Theoretical and Computational Fluid Dynamics*, Vol. 20, No. 3, May 2006, pp. 181–195.

[9] Hassan, E., Aono, H., Boles, J., Davis, D., and Shyy, W., "Multi-Scale Turbulence Model Simulation of Supersonic Crossflow," AIAA Paper 2010–111, Orlando, FL, January 2011.

[10] Lin, K.-C., Ryan, M., Carter, C., Gruber, M., and Raffoul, C., "Raman Scattering Measurements of Gaseous Ethylene Jets in Mach 2 Supersonic Crossflow," *Journal of Propulsion and Power*, Vol. 26, No. 3, May–June 2010, pp. 503–513.

[11] Gruber, M. R., Nejad, A. S., Chen, T. H., and Dutton, J. C., "Transverse Injection from Circular and Elliptic Nozzles into a Supersonic Crossflow," *Journal of Propulsion and Power*, Vol. 16, No. 3, 2000, pp. 449–457.

[12] Mathur, T., Streby, G., Gruber, M., Jackson, K., Donbar, J., Donaldson, W., Jackson, T., Smith, C., and Billig, F., "Supersonic Combustion Experiments with a Cavity-Based Fuel Injector," AIAA Paper 99–2102, Los Angeles, CA, June 1999.

[13] Gruber, M. R., Baurle, R. A., Mathur, T., and Hsu, K.-Y., "Fundamental Studies of Cavity-Based Flameholder Concepts for Supersonic Combustors," *Journal of Propulsion and Power*, Vol. 17, No. 1, 2001, pp. 146–153.

[14] Davis, D. L., *Numerical Analysis of Two and Three Dimensional Recessed Flame Holders for Scramjet Applications*, Ph.D. thesis, Air Force Institute of Technology Air University, September 1996.

[15] Kim, K. M., Baek, S. W., and Han, C. Y., "Numerical Study on Supersonic Combustion with Cavity-Based Fuel Injection," *International Journal of Heat and Mass Transfer*, Vol. 47, 2004, pp. 271–286.

[16] http://legacy.mae.ncsu.edu/research/cfd_lab/index.html.

[17] Boles, J. A., Choi, J.-I., Edwards, J. R., and Baurle, R. A., "Multi-Wall Recycling / Rescaling Method for Inflow Turbulence Generation," AIAA Paper 2010–1099, Orlando, FL, January 2010.

[18] Edwards, J. R., "A Low-Diffusion Flux-Splitting Scheme for Navier-Stokes Calculations," *Computers & Fluids*, Vol. 26, No. 6, 1997, pp. 635–659.

[19] Colella, P. and Woodward, P. R., "The Piecewise Parabolic Method (PPM) for Gas-Dynamical Simulations," *Journal of Computational Physics*, Vol. 54, 1984, pp. 174–201.

[20] http://metacomptech.com.

[21] Gruber, M. R. and Nejad, A. S., "New Supersonic Combustion Research Facility," *Journal of Propulsion and Power*, Vol. 11, No. 5, 1995, pp. 1080–1083.

[22] Boles, J., Milligan, R., Hagenmaier, M., Eklund, D., and Edwards, J., "Hybrid Large-Eddy Simulation / Reynolds-Averaged Navier-Stokes Simulation of Sonic Injection into Mach 2 Crossflow," AIAA Paper 2011–769, Orlando, FL, January 2011.

[23] Fric, T. F., "Skewed Shear Layer Mixing Within a Duct," AIAA Paper 95-0869, Reno, NV, January 1995.

[24] Etheridge, S., Carter, C. D., and Lee, J., "Characterization of Supersonic Flow Interaction with Shockwaves Using Laser-based Diagnostics," 2012, to be presented at 2012 Joint Propulsion Conference.

[25] Rasmussen, C. C., Driscoll, J. F., Hsu, K.-Y., Donbar, J. M., Gruber, M. R., and Carter, C. D., "Stability limits of cavity-stabilized flames in supersonic flow," *Proceedings of the Combustion Institute*, Vol. 30, 2005, pp. 2825–2833.

[26] Baurle, R. A. and Eklund, D. R., "Analysis of Dual-Mode Hydrocarbon Scramjet Operation at Mach 4 – 6.5," AIAA Paper 2001–3299, Salt Lake City, UT, July 2001.

LIST OF ACRONYMS, ABBREVIATIONS, AND SYMBOLS

Acronyms

AFRL — Air Force Research Laboratory

AOA — angle of attack

BSL — baseline

CFD — computational fluid dynamics

DNS — direct numerical simulation

LDFSS — Low-Diffusion Flux-Splitting Scheme

LES — large eddy simulation

LFL — lower flammability limit

NO-PLIF — nitrous oxide-planar laser-induced fluorescence

OH-PLIF — OH planar laser-induced fluorescence

PPM — Piecewise Parabolic Method

RANS — Reynolds-averaged Navier-Stokes

SBLI — shockwave-boundary layer interaction

slpm — standard liters per minute

Roman Symbols

c — time-averaged mixture fraction

$\bar{c}$ — planar- and time-averaged mixture fraction

D — jet diameter

k — turbulent kinetic energy

M — mixedness parameter

Pr_t — turbulent Prandtl number

q — momentum flux ratio

Sc_t — turbulent Schmidt number

u_τ — friction velocity

y^+ dimensionless, sublayer-scaled, distance, $u_\tau y/\nu$, at first grid point away from surface

Y_f fuel mass fraction

Y_t fuel mass fraction threshold

Greek Symbols

α blanking variable for plume edge calculation

ϵ turbulence dissipation

ν kinematic molecular viscosity

ρ_f species density of fuel

Φ equivalence ratio